Electronic Supplementary Material (ESI) for ChemComm.

Supporting Information

Tunneling and Thermoelectric Characteristics of *N*-Heterocyclic Carbene-based Large-Area Molecular Junctions

Seohyun Kang, Sohyun Park, Hungu Kang, Soo Jin Cho, Hyunsun Song and Hyo Jae Yoon*

Department of Chemistry, Korea University, Seoul, 02841, Korea

Corresponding author's email: hyoon@korea.ac.kr

Table of Contents

1. Experimental Details

1.1 Materials and Characterization

All reagents were purchased from Sigma-Aldrich, Alfa Aesar, and TCI and used as supplied unless otherwise specified. All organic solvents were purchased from Sigma-Aldrich and Daejung while water was purified using an Aqua MAX-Basic System (deionized water, the electrical resistivity of which is ~18.2 MΩ·cm). High purity eutectic gallium-indium (EGaIn; 99.99%) was obtained from Sigma-Aldrich and used as supplied. *N*-Heterocyclic carbene (NHC) molecules were synthesized following Schemes S1. Compounds **S1**-**S3** were synthesized following the previously reported procedures.[1-4] Gold thin films (300 nm) were deposited onto silicon wafer (100 mm in diameter; 1–10 ohm-cm, 525 ± 50 microns thick) by e-beam evaporator (ULVAC). Photo-curable polymer was purchased from Norland (NOA81) and used as supplied.

^{1}H and ^{13}C NMR spectra were recorded on a Bruker FT-NMR Advance-500 using $CDCl_3$, acetone-d_6 or methanol-*d* as a solvent and residual solvents as an internal standard. Chemical shifts are expressed in parts per million (ppm) relative to internal TMS, and coupling constants (*J*) are in Hertz. Mass spectrometry (ESI-QTOF) measurements were recorded on a Bruker compact Q-TOF MS. All X-ray photoelectron spectroscopy (XPS) and ultraviolet photoelectron spectroscopy (UPS) measurements were carried out on a Thermo Thetaprobe with a monochromated Al Kα and He I source. Junction measurements at variable temperatures were carried out in a cryogenic probe station (PS-CG2ST, MODUSYS). An atomic force microscopy (AFM) (Bruker AFM Multimode model) was used for Kelvin probe force microscopy (KPFM) measurements and topography analysis.

1.2 Synthesis

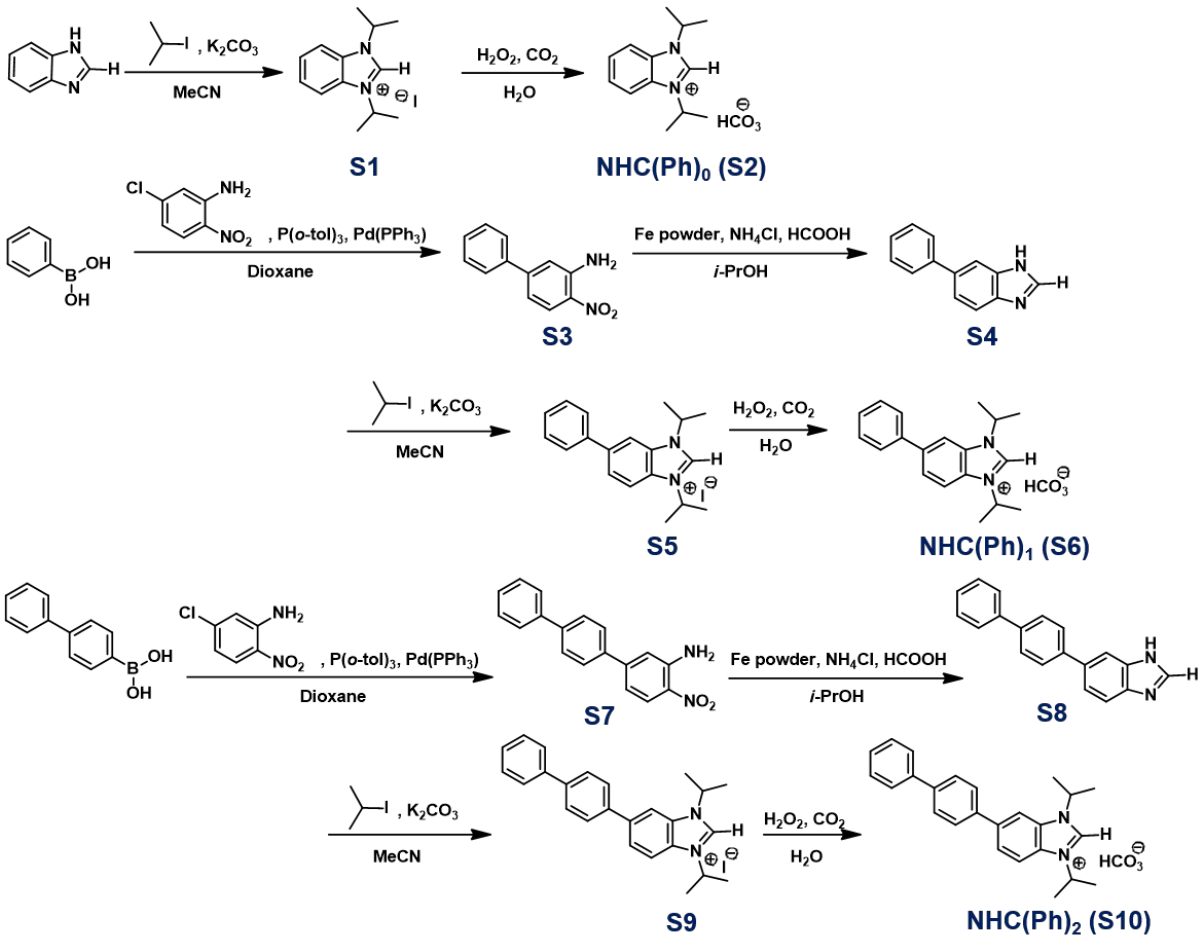

Scheme S1. Synthetic scheme of oligophenylene-NHC molecules, $NHC(Ph)_n$ (n=0,1,2; **S2, S6 and S10**).

1,3-Diisopropyl-1H-benzo[d]imidazol-3-ium iodide (S1)

A 2-neck 100 mL round bottom flask equipped with a Teflon coated stir bar, reflux condenser with a gas inlet adapter, and rubber septum was charged with 1*H*-benzo[d]imidazole (0.60 g, 3.6 mmol), K2CO3 (1.00 g, 7.2 mmol) and 20 mL of acetonitrile. The reaction mixture was sparged with N2 while stirring vigorously for 30 min. 2-Iodopropane (2.5 mL, 25 mmol) was then added using a N2 flushed syringe. The reaction mixture was refluxed at 90°C and stirred for 48 h. The reaction mixture was then cooled to room temperature and all volatiles were

removed *in vacuo*. The flask was opened to air, the solid residue was sonicated in 50 mL of DCM for 10 min, and filtered through a pad of Celite over a medium porosity frit. The filter cake was washed with DCM. The DCM filtrate was concentrated by rotary evaporation and ethyl acetate was added to induce precipitation. The suspension was then sonicated for 1 h, the solid was collected by filtration and washed with ethyl acetate and diethyl ether. The solid was then dried *in vacuo* to yield **S1** as an off-white powder. (Yield: 893 mg, 87%) The analytical data for this compound were in excellent agreement with the reported data.[1]

1,3-Diisopropyl-1*H*-benzo[*d*]imidazol-3-ium bicarbonate (S2)

A 50 mL round bottom flask capped with a rubber septum and containing a needle for ventilation and a glass pipette for addition of gaseous carbon dioxide was charged with a clear colorless solution of 1,3-diisoproplylbenzimidazolium iodide (**S1**) (500 mg, 1.5 mmol) in deionized water (30 mL). CO_2 was bubbled through this solution for 1 min, after which time hydrogen peroxide (225 µL (35% w/v), 2.25 mmol in 0.5 mL water) was injected. Vigorous CO_2 bubbling was maintained for 1 h under stirring during which time the solution turned yellow and then brown until the formation of a purple precipitate was detected. The mixture was filtered by vacuum filtration and washed with 3 mL of water resulting in a clear colorless filtrate solution, leaving the insoluble iodine as a violet solid precipitate. Water was removed by flushing air overnight over the surface of the solution then the product was dried under high vacuum for 2 h to give a white solid. The resulting solid was triturated and sonicated in acetone (3 × 3 mL), which was then decanted off. Subsequent drying under vacuum afforded the desired product as a white powder (645 mg, 89% yield). It is worthy to note that this procedure cannot be applied in organic solvents such as methanol due to the solubility of the formed iodine and its disproportionation under this basic condition. To test complete removal of iodine, a qualitative silver nitrate test was performed where one drop

from the reaction aliquot was mixed with excess aqueous silver nitrate (1 M) solution. In cases where incomplete exchange was observed, a yellow precipitate of silver iodide formed that persisted upon the addition of nitric acid. When iodide was completely exchanged, a white precipitate of silver bicarbonate formed that became colorless upon addition of a solution of 1M nitric acid. The analytical data for this compound were in excellent agreement with the reported data.[2]

4-Nitro-[1,1'-biphenyl]-3-amine (S3)

This compound was synthesized following a modified literature procedure.[2] A 100 mL 2-neck round bottom flask equipped with a Teflon coated stir bar, reflux condenser with a gas inlet adapter, and rubber septum was charged with phenylboronic acid (1.00 g, 8.2 mmol), 5-chloro-2-nitroaniline (1.09 g, 6.3 mmol) and tri(*o*-tolyl)phosphine (0.576 g, 1.9 mmol). The flask was evacuated and refilled with N_2. In a separate flask, a mixture of 30 mL of dioxane and 10 mL of 2.0 M aqueous K_2CO_3 was sparged with N_2 for 30 min. The mixture was transferred to the 2-neck flask using a cannula and $Pd(PPh_3)_4$ (0.47 g, 0.41 mmol) was added to the flask. The reaction was stirred under reflux for 18 h. The flask was then opened to air and dioxane was removed via rotary evaporation. Ethyl acetate (100 mL) was added to the flask, and the mixture was washed with water and with brine. The organic phase was dried over $MgSO_4$ and purified by silica gel flash column chromatography, eluting with a 20% ethyl acetate in hexanes gradient. **S3** was obtained as a yellow crystalline solid. The analytical data for this compound were in excellent agreement with the reported data.[4]

6-Phenyl-1*H*-benzo[*d*]imidazole (S4)

This compound was synthesized following a modified literature procedure.[2] A 250 mL 2-neck round bottom flask equipped with a Teflon coated stir bar, reflux condenser with gas inlet adapter, and rubber septum, was charged with **S3** (0.5 g, 2.33 mmol), Fe powder (1.30 g, 23.3 mmol), and ammonium chloride (1.25 g, 23.3 mmol). The flask was evacuated and refilled with N2. In a separate 100 mL round bottom flask equipped with a stir bar and rubber septum, 7 mL of formic acid and 10 mL of isopropanol were sparged with N2 for 15 min. After sparging, the formic acid and isopropanol solution was added to the flask containing **S3**, Fe powder, and ammonium chloride *via* cannula. Benzene (100 µL) was then added to the reaction to aid solubilizing the amine. The reaction mixture was heated to reflux at 80°C and stirred under N_2 for 3 h. The reaction mixture underwent several color changes finally ending in a light yellow-green with a large amount of gray precipitate. After 3 h, the reaction mixture was cooled to room temperature, opened to air and filtered through a pad of Celite over a medium porosity frit. The filter cake was washed with isopropanol. The combined filtrate was evaporated to dryness via rotary evaporation, leaving a sticky solid. Saturated aqueous NaHCO3 solution was slowly added to the solid residue until a neutral pH was obtained. The reaction mixture was then transferred to a separatory funnel and extracted with chloroform. The combined extracts were dried over MgSO4, filtered, and the solvent was removed via rotary evaporation to yield **S4** as a sticky, brown, foamy solid. (Yield: 342 mg, 75%) ^{1}H NMR (500 MHz, DMSO): δ ppm 12.43 - 12.57 (m, 1 H) 8.25 (br. s., 1 H) 7.91 (s, 1 H) 7.72 - 7.76 (m, 1 H) 7.69 (d, J=7.32 Hz, 2 H) 7.50 - 7.64 (m, 1 H) 7.43 - 7.49 (m, 2 H) 7.30 - 7.37 (m, 1 H) ^{13}C NMR(500 MHz, DMSO): δ 132.76, 132.01, 131.93, 130.76, 129.50, 129.37, 129.29, 129.19, 127.42, 127.23, 126.85. MS (ESI) *m/z*: $[M+H]^+$ calcd for $C_{13}H_{11}N_2$: 195.0917; found: 195.0915.

1,3-Diisopropyl-6-phenyl-1H-benzo[d]imidazol-3-ium iodide (S5)

This compound was synthesized following the same procedure as **S1**, starting from **S4** (685 mg, 3.5 mmol) with the following modifications. The reaction mixture was heated to reflux and stirred until consumption of the starting benzimidazole material, as determined by NMR (typically 48-96 h). An additional 4 equivalents of 2-iodopropane was added after 48 h if the reaction was not completed. The product was precipitated using a 50:50 mixture of ethyl acetate and diethyl ether. The suspension was ten sonicated for 1 h, the solid was collected by filtration and washed with ethyl acetate and diethyl ether. **S5** was obtained as an off-white powder (Yield: 542 mg, 38%). ^{1}H NMR (500 MHz, $CDCl_3$): δ ppm 11.12 (s, 1 H) 7.86 (d, *J*=0.92 Hz, 1 H) 7.84 (dd, *J*=2.75, 1.22 Hz, 2 H) 7.59 - 7.63 (m, 2 H) 7.51 - 7.56 (m, 2 H) 7.45 - 7.50 (m, 1 H) 5.19 - 5.29 (m, 2 H) 1.91 (dd, *J*=6.87, 4.73 Hz, 13 H). ^{13}C NMR (500 MHz, $CDCl_3$): *δ* 141.22, 139.13, 132.04, 131.96, 129.95, 129.23, 128.53, 127.57, 114.20, 111.80, 52.61, 52.37, 22.28, 22.25. MS (ESI) *m/z*: $[M-I]^+$ calcd for $C_{19}H_{23}N_2$: 279.1856; found: 279.1890

1,3-Diisopropyl-6-phenyl-1*H*-benzo[*d*]imidazol-3-ium bicarbonate (S6)

This compound was synthesized following the same procedure as **S2**, starting from **S5** (542 mg, 1.33 mmol) with the following modifications. The solvent mixture used for the reaction is 15 mL of deionized water and 10 mL of dry THF. After 3 h, the reaction mixture was dried under high vacuum to evaporate the solvent and added water to solve the solid residue. The reaction mixture was then transferred to a separatory funnel and extracted with ethyl acetate. The resulting water layer was dried under high vacuum to give a white solid. The resulting solid was triturated and sonicated in ethyl acetate, which was then decanted off. Subsequent drying under vacuum afforded the desired product as a white powder. (Yield: 354 mg, 72%) ^{1}H NMR (500 MHz, MeOD-d_4): δ ppm 8.22 (s, 1 H) 8.10 (d, *J*=8.54 Hz, 1 H) 7.99 (d,

J=10.38 Hz, 1 H) 7.76 (d, *J*=7.32 Hz, 2 H) 7.53 (t, *J*=7.63 Hz, 2 H) 7.42 - 7.48 (m, 1 H) 5.07 - 5.21 (m, 2 H) 1.77 (dd, *J*=6.71, 2.14 Hz, 12 H). ^{13}C NMR (500 MHz, MeOD-d_4): δ 164.67, 161.26, 143.66, 142.04, 137.53, 130.49, 129.63, 128.78, 112.74, 110.84, 108.60, 52.87, 52.78, 22.47, 22.40. MS (ESI) *m/z*: $[M\text{-}HCO_3]^+$ calcd for $C_{19}H_{23}N_2$: 279.1856; found: 279.1890.

4-Nitro-[1,1':4',1''-terphenyl]-3-amine (S7)

This compound was synthesized following the same procedure as **S3**, starting from 4-biphenylboronic acid (1 g, 5.05 mmol) and 5-chloro-2-nitroaniline (676 mg, 3.88 mmol) with the following modifications. The solvent mixture used for the reaction is 80 mL of dioxane, 100 µL of benzene and 20 mL of a 2.0 M aqueous K_2CO_3. After stirring under reflux for 18 h, the reaction mixture was hot filtered and dioxane was removed by rotary evaporation. The precipitated solid was collected by filtration, washed with water, and diethyl ether. The solid was then redissolved in 150 mL of DCM, dried over MgSO4, filtered, and the solvent was removed by rotary evaporator. The resulting solid was dried *in vacuo*. **S7** was obtained as a bright yellow solid. (Yield: 804 mg, 55%) ^{1}H NMR (500 MHz, $CDCl_3$-*d*) δ ppm 8.21 (d, *J*=8.85 Hz, 1 H) 7.62 - 7.72 (m, 6 H) 7.48 (t, *J*=7.63 Hz, 2 H) 7.36 - 7.42 (m, 1 H) 7.04 (d, *J*=1.83 Hz, 1 H) 6.99 (dd, *J*=8.85, 2.14 Hz, 1 H). ^{13}C NMR (500 MHz, $CDCl_3$): δ 148.02, 144.85, 141.78, 140.20, 128.91, 127.74 127.56, 127.07, 126.93, 116.30, 116.27. MS (ESI) *m/z*: $[M+Na]^+$ calcd for $C_{18}H_{14}N_2NaO_2$: 313.0947; found: 313.0947.

6-([1,1'-Biphenyl]-4-yl)-1*H*-benzo[d]imidazole (S8)

This compound was synthesized following the same procedure as **S4**, starting from **S7** (604 mg, 2.08 mmol) with the following modifications. Benzene (300 µL) was added to the reaction to aid solubilizing the amine. After refluxing for 12 h, the mixture was hot filtered. The solid product was washed with ethyl acetate to remove excess starting material. **S8** was

obtained as a light yellow-orange powder. (Yield: 500 mg, 89%) ^{1}H NMR (500 MHz, Acetone-d_6): δ ppm 8.20 (s, 1 H) 8.11 (s, 1 H) 7.79 - 7.83 (m, 2 H) 7.76 - 7.79 (m, 2 H) 7.74 (d, *J*=8.24 Hz, 2 H) 7.60 (d, *J*=8.54 Hz, 1 H) 7.49 (t, *J*=7.63 Hz, 2 H) 7.38 (t, *J*=6.87 Hz, 1 H). ^{13}C NMR (500 MHz, $CDCl_3$): *δ* 163.42, 143.06, 141.83, 141.48, 140.25, 135.94 133.82, 129.85, 128.56, 128.26, 128.23, 127.66, 122.51. MS (ESI) *m/z*: $[M+H]^+$ calcd for $C_{19}H_{15}N_2$: 271.1230; found: 271.1231.

6-([1,1'-Biphenyl]-4-yl)-1,3-diisopropyl-1*H*-benzo[*d*]imidazol-3-ium iodide (S9)

This compound was synthesized following the same procedure as **S2**, starting from **S8 (**500 mg, 1.85 mmol) with the following modifications. The reaction was stirred under reflux until consumption of the starting benzimidazole, as determined by NMR (typically ~72 h). An additional 4 equivalents of 2-iodopropane were added after 48 h. The product was precipitated using ethyl acetate. **S9** was obtained as a white powder (Yield: 184 mg, 21%). ^{1}H NMR (500 MHz, $CDCl_3$) δ ppm 11.05 (s, 1 H) 7.88 - 7.93 (m, 2 H) 7.83 - 7.87 (m, 1 H) 7.76 (m, *J*=8.24 Hz, 2 H) 7.70 (m, *J*=8.54 Hz, 2 H) 7.64 - 7.67 (m, 2 H) 7.50 (t, *J*=7.63 Hz, 2 H) 7.38 - 7.44 (m, 1 H) 5.21 - 5.30 (m, 2 H) 1.93 (t, *J*=7.20 Hz, 12 H). ^{13}C NMR (500 MHz, $CDCl_3$): *δ* 141.59, 140.82, 140.04, 137.93, 131.58, 130.02, 128.96, 127.98, 127.06, 126.76, 114.21, 111.71, 52.74, 52.49, 22.33, 22.28. MS (ESI) *m/z*: $[M-I]^+$ calcd for $C_{25}H_{27}N_2$: 355.2169; found: 355.2169.

6-([1,1'-Biphenyl]-4-yl)-1,3-diisopropyl-1*H*-benzo[*d*]imidazol-3-ium bicarbonate (S10)

This compound was synthesized following the same procedure as **S2**, starting from **S9** (184 mg, 0.38 mmol) with the following modifications. The solvent mixture used for the reaction is 15 mL of deionized water and 10 mL of dry THF. After 3 h, the reaction mixture was dried

under high vacuum to evaporate the solvent and added water to solve the solid residue. The reaction mixture was then transferred to a separatory funnel and extracted with ethyl acetate. The resulting water layer was dried under high vacuum to give a white solid. The resulting solid was triturated and sonicated in ethyl acetate, which was then decanted off. Subsequent drying under vacuum afforded the desired product as a white powder (Yield: 107 mg, 68%). ^{1}H NMR (500 MHz, Acetone-d_6) δ ppm 8.45 (s, 1 H) 8.22 - 8.27 (m, 1 H) 8.06 - 8.11 (m, 1 H) 7.91 - 7.97 (m, 2 H) 7.81 - 7.87 (m, 2 H) 7.71 - 7.77 (m, 2 H) 7.48 - 7.54 (m, 2 H) 7.38 - 7.43 (m, 1 H) 5.24 - 5.43 (m, 2 H) 1.84 (t, *J*=1.00 Hz, 11 H). ^{13}C NMR (500 MHz, MeOD-d_4): δ 141.64, 140.87, 140.09, 137.99, 131.63, 130.07, 129.01, 128.04, 127.11, 126.82, 114.26, 111.76, 52.79, 52.54, 22.39, 22.34. MS (ESI) *m/z*: $[M\text{-}HCO_3]^+$ calcd for $C_{25}H_{27}N_2$: 355.2169; found: 355.2170.

1.3 SAM Preparation

We prepared SAMs following the procedure reported previously.[2, 5] Briefly, ethanol (anhydrous, 99.9%) solution (2 mM) containing an NHC precursor ($NHC(Ph)_nHCO_3$) was added to a vial. A freshly prepared template-stripped gold (Au^{TS}) chip was rinsed with pure ethanol, and placed to the solution with the exposed metal face up. After 1-3 h incubation at room temperature, the SAM-bound Au^{TS} chip was removed from the solution and rinsed by repeatedly dipping the chip into clean ethanol (3 × 1 mL). The solvent on the SAM was then evaporated in air for a few seconds.

2. Electrical Measurements

Tethered junction formation and measurements were done following the method reported in the literature.[6, 7] Untethered junction formation and low temperature experiments were done following the method reported in the literature.[8]

3. Thermoelectric Measurements and Analysis

Thermoelectric junction measurements were conducted following the previously reported procedure.[9] In a typical experiment, we confirmed that the air temperature of the laboratory was constant prior to the creation of ΔT across a junction. Typical air temperature in the laboratory and its variation were 294.1 – 294.5 K and less than ± 0.1 K, respectively. To create temperature difference, the SAM-bound Au^{TS} was placed on a hot chuck, which was heated from 290 K to 298 K. At each temperature, we waited until the temperature measured on the bottom-electrode thermocouple was stabilized. Then using a micromanipulator, a conical tip of EGaIn was gently brought into contact with the surface of SAM, and output voltage was measured. To analyze thermopower of junctions, we followed the previous method.[10, 11] Thermopower reflects the slope of ΔV vs. ΔT, and ΔT occurs across the junction. When a SAM is not present, ΔT occurs across the EGaIn tip and the tungsten (W) ground electrode. When a SAM is present, ΔT occurs across the molecule and the W electrode. Thus, using the equations in the Figure S5, we were able to estimate thermopower of SAMs. For the Seebeck coefficients of EGaIn and Ga_2O_3, we used the previously measured values.[9] The potential uncertainty of temperature differential has been described elsewhere.[9]

4. Simulation of *I-V* Curves with a Single Lorentzian-based Transmission Function

We simulated current-voltage (*I-V*) curves with Landauer formula (Eq. S1) and a single Lorentzian model-based transmission function (Eq. S2):[12-14]

$$I = \frac{2e}{h}\int_{-eV/2}^{eV/2} T(E)\ dE \qquad \text{Eq. S1}$$

$$T(E) = (\Gamma^2/4)\ /((E - \varepsilon - \alpha eV)^2 + \Gamma^2/4) \qquad \text{Eq. S2}$$

Here, e is the fundamental unit of charge, h is Planck's constant, and V is the applied voltage. The transmission function $T(E)$ is assumed to be a single Lorentzian for the sake of simplicity. $T(E)$ relies on the energy (E), the molecular energy level (ε) and the molecule-electrode coupling strength (Γ).[13] For simulation, we used the literature value of Γ_L corresponding to C_{sp2}-Au (0.50 eV)[15] for all the junctions. This was plausible considering that all the junctions have the same bottom-interface and are based on the covalent bond between gold atom and sp^2 carbon. We used the value Γ_R=0.050 eV[16] for all the junctions, assuming that the junctions have the same molecule-top electrode interface. For the molecular orbital energy, we used the valence band edge energy estimated by UPS.

Figure S14 shows the plot of transmission coefficient against the energy offset between E_F and HOMO energy level (ε_{HOMO}; -8.14, -6.91 and -5.46 eV for n=0,1,2, respectively; see the Supporting Information for details) estimated by UPS. As the number of phyenylene units increased, the energy offset decreased. We were able to fit the experimentally measured data with the simulation data using the transmission coeffcient (Figure S17). From this fitting we were able to estimate the dimensionless Stark coefficient, α, which reflects the shift of the molecular level relative to the electrode chemical potential under an external bias.[16, 17] If α=0, the relative alingment of molecular energy level does not change by the external bias, and thus no significant rectification is usually expected. Our fitting shows that α=0.06 for the SAMs, and this small value explains the modest rectification raitos we observed. This small value is similar to the analogous junction that does not show significant rectification.[16] Note that our modeling focused on fitting of relative trends of

conductance and rectification ratio against the molecular length, rather than on absolute values of tunneling current.

5. Seebeck Coefficient Modeling with Single Lorentzian-shaped Transmission Function

Our modeling of Seebeck coefficient was conducted based on the previously reported methods.[18, 19] For modeling of Seebeck coefficient, we used the identical transmission function and the Γ_L and Γ_R values used for the *I-V* modeling. The Landauer formula[18, 20] can be used to relate *S* to the transmission function of the junction as follows:

$$S = -\frac{\pi^2 k_B{}^2 T}{3e} \frac{\partial \ln(\tau(E))}{\partial E}\Big|_{E=E_F} \qquad \text{Eq. S3}$$

where *e* is the charge of a proton, k_B is the Boltzmann constant, and *T* is the average absolute temperature of the junction (in our case, *T* was 295 K). We read *S* value at the Fermi energy of EGaIn (E_F= 4.2 eV).[7] The measured values are 3.5, 5.3, 11.9 μV/K for $NHC(Ph)_0$ $NHC(Ph)_1$ and $NHC(Ph)_2$, respectively. We found that the theoretical value of *S* increases with the number of aromatic rings.

6. Further Discussions on Characterizations and Modeling

6.1 XPS Measurements

The XPS measurements were carried out on a Thetaprobe (Thermo) with a monochromated Al Ka (1486.6 eV) source. The measurements were done at room temperature in a vacuum of 6.7×10^{-8} Pa. The binding energies were calibrated by setting Au 4f of bulk metals to values 84.0 eV. The XPS Au4f, C1s, N1s, and O1s lines were detected to study the $NHC(Ph)_n/Au^{TS}$ (n=0, 1, 2) SAMs. The peak shapes of the core level photoelectron spectra were analyzed with a XPS Peak Fit program. A Shirley-type background correction was used. The single

binding energies of N1s were observed at 401.3 – 402.5 eV for our SAMs. The C1s peaks were deconvoluted into three signals at 289.5 – 290.0 eV, 286.0 – 286.5 eV and 285.0 – 285.8 eV, which corresponded to C-O, C-N, and C-C/C=C, respectively. As shown in Figure S6-S8 and Table S3, the atomic percentages corresponding to C-C/C=C and C-N increased and decreased, respectively, as the number of phenylene units increased. On the other hand, the atomic percentage corresponding to C-O remained relatively constant. These observations confirm the formation and thickness control of NHC monolayers on Au^{TS}, and the presence of byproducts (CO_2 and/or H_2O) resulting from the decomposition of NHC hydrogen carbonate molecule (as a precursor) upon the chemisorption.[2, 5, 21]

6.2 UPS Measurements

UPS were carried out on Thetaprobe (Thermo) to determine the Fermi level and the HOMO level of Au^{TS}/$NHC(Ph)_n$ (n=0, 1, 2) SAMs. The HOMO level was determined by the following equation, HOMO level = $h\nu - (E_{cutoff} - E_{onset})$, where $h\nu$ is incident photon energy (21.2 eV) of He I source, the high binding energy cutoff (E_{cutoff}) and HOMO region (E_{onset}) are the turning points shown in Figure S9. From the E_{onset} analysis, we estimated energy levels of HOMO (ε_{MO}) for $NHC(Ph)_0$ $NHC(Ph)_1$ and $NHC(Ph)_2$ SAMs on Au^{TS}: -8.14, -6.91 and -5.46 eV, respectively. Similarly, from the E_{cutoff} analysis, we estimated the values of work function (WF) for the SAM-bound Au^{TS} chips: 3.45, 4.04, 3.77 eV for n=0,1,2, respectively. The significant reduction of WF relative to the polycrystalline gold substrate (the Au^{TS} we used) observed in our SAMs is remarkable and cannot be easily achieved by the chemisorption of thiol derivatives onto gold. The similar observation has been previously reported.[22]

6.3 Static and Dynamic Contact Angle Measurements

The formation of Au^{TS}/NHC$(Ph)_n$ (n=0, 1, 2) SAMs was evaluated with water contact angle measurements. Contact angle for each molecule was averaged from 12 separate measurements. Bare Au^{TS} showed an average contact angle of 50° ± 4, and the NHC$(Ph)_n$ SAM-bound Au^{TS} chips showed contact angles (~50° – 60°) similar to that of bare Au^{TS}. This is due to the presence of polar nitrogen atoms in the surface-exposed NHC moiety (see Figure S10). The contact angles of our SAMs were lower than conventional CH_3-terminated SAMs (105° ± 0.5). No significant difference in dynamic contact angle was observed across different number of phenylene units. The similarity in static and dynamic contact angle data indicate that there were no significant differences in the surface energy and roughness across different NHC molecules.

6.4 Kelvin probe force microscopy (KPFM) Measurements

We carried out KPFM measurements in ambient conditions using a Bruker AFM Multimode model in amplitude modulated KPFM. Pt/Ir coated conductive probes (SCM-PIT-V2, spring constant 3 N/m, resonant frequency 75 kHz, Bruker) were calibrated on freshly cleaved highly oriented pyrolytic graphite (HOPG) to determine the work function of the tip (Φ_{tip}). Topography and KPFM data were obtained simultaneously using a standard two-pass procedure, where a topographic line is first acquired in tapping mode and a KPFM line is secondly acquired in a lift mode. In the lift mode, the tip scans at a constant distance of 80 nm above the sample surface to ensure that electrostatic forces are dominating. In KPFM mode, the applied AC voltage has an amplitude of 500 mV at a frequency close to the resonance frequency of the cantilever (about 70 kHz). KPFM images of the sample surface were acquired at a probe scan rate of 0.5 Hz with scan size of 1 μm and 512 samples per line over five different regions. The subsequently measured, averaged contact potential difference (CPD) values between the tip and NHC SAM samples (Φ_{sample}) were used to calculate their

respective work functions using below equation based on the work function of the tip. See the following equations.

$$\Phi_{tip} = \Phi_{HOPG} - V_{HOPG,\,CPD} \quad (\Phi_{HOPG} = 4.50\ eV)$$

$$= 4.795\ eV$$

$$\therefore\ \Phi_{sample} = \Phi_{tip} + V_{sample,\,CPD}$$

The trends of WF were related to the packing density of molecules. In the XPS analysis, N 1s versus Au 4f was the highest at n=1, indicating the highest packing density among the three SAMs. The well packed structure could lead to depolarization of molecules by interaction with neighboring ones inside the monolayer.[23-25] Hence, given that the degree of WF change depends on the surface dipole, the small reduction of WF relative to the bare gold for the tightly packed monolayer is plausible. The observed difference in WF did not determine the length dependence of tunneling current density (consistent with other results in the literature[23, 26-29]) and thermopower of NHC-based molecular junctions.

7. Supplementary Figures and Tables

Table S1. Summary of Tunneling Junction Measurements

Tunneling Characteristics					
SAM	$N_{junction}$[a]	N_{trace}[b]	Yield (%) [c]	$\log\|J(-1V)\|_{mean} \pm \sigma_{\log\|J\|}$ ($\log\|J(-1V)\|_{median}$)	$\log\|J(+1V)\|_{mean} \pm \sigma_{\log\|J\|}$ ($\log\|J(+1V)\|_{median}$)
$NHC(Ph)_0$	27	468	88	-0.9 ± 0.4 (-0.9)	-0.7 ± 0.6 (-0.7)
$NHC(Ph)_1$	20	374	89	-1.7 ± 0.5 (-1.7)	-1.4 ± 0.6 (-1.7)
$NHC(Ph)_2$	23	404	92	-2.4 ± 0.5 (-2.3)	-2.0 ± 0.6 (-1.9)

[a] The number of working junctions
[b] The number of *J-V* traces
[c] The yield of working junctions

Table S2. Summary of Thermoelectric Junction Measurements

Thermoelectric Characteristics							
SAM	ΔT	N_{tip}[a]	$N_{junction}$[b]	N_{points}[c]	Yield (%) [d]	$\Delta V_{mean} \pm \sigma_{\Delta V}$	S_{SAM} (μV/K)
$NHC(Ph)_0$	2 K	8	30	2280	91	-40 ± 9	9.1 ± 2.1
	4 K	8	30	2280	94	-63 ± 9	
	6 K	8	31	2356	91	-73 ±11	
$NHC(Ph)_1$	2 K	8	30	2280	94	-47 ± 11	10.0 ± 0.9
	4 K	9	33	2508	92	-65 ± 9	
	6 K	8	29	2204	91	-74 ± 16	
$NHC(Ph)_2$	2 K	9	34	2584	92	-43 ± 8	12.5 ± 0.5
	4 K	10	39	2964	91	-68 ± 12	
	6 K	9	34	2584	92	-89 ± 15	

[a] The number of EGaIn tip used.
[b] The number of working junctions
[c] The number of ΔV data points
[c] The yield of working junctions

Table S3. Summary of Deconvolution of C1s peaks in XPS High Resolution Spectra

C species	$NHC(Ph)_0$	$NHC(Ph)_1$	$NHC(Ph)_2$
C-C/C=C	45.5	59.1	66.9
C-N	44.9	28.2	23.0
C-O	9.56	12.7	10.1
Total	100	100	100

Table S4. Summary of Dynamic Contact Angle Measurements[a]

	θ_a (rad)[b]	θ_r (rad)[c]	$\cos\theta_a$	$\cos\theta_b$	$\Delta\cos(\theta_a-\theta_r)$ $(=\Delta\cos\theta_d)$
$NHC(Ph)_0$	1.04 ± 0.08	0.89 ± 0.11	0.51 ± 0.07	0.62 ± 0.08	0.12 ± 0.05
$NHC(Ph)_1$	1.07 ± 0.06	0.93 ± 0.06	0.48 ± 0.05	0.59 ± 0.05	0.12 ± 0.06
$NHC(Ph)_2$	0.89 ± 0.09	0.73 ± 0.11	0.62 ± 0.07	0.74 ± 0.07	0.11 ± 0.06

[a] Averaged from 12 separate measurements
[b] advancing contact angles
[c] receding contact angles

Figure S1. Log|*J*|-*V* traces of $Au^{TS}/NHC(Ph)_n//Ga_2O_3/EGaIn$ junctions measured in the voltage range from 0 V to ±1.0 V: (a) n=0 (b) n=1 (c) n=2.

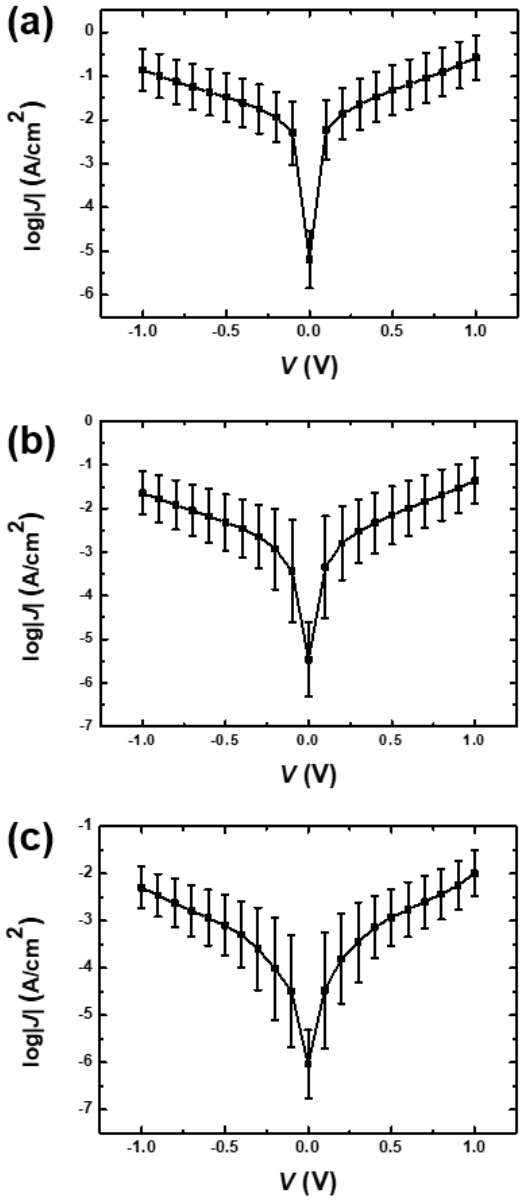

Figure S2. Data of low temperature (from 113 to 293 K) experiments for $Au^{TS}/NHC(Ph)_0//Ga_2O_3/EGaIn$ junction. a) *J-V* traces measured at ±1.0 V; (b) log|*J*|-V traces measured at ±1.0 V; (c) the corresponding Arrhenius plot.

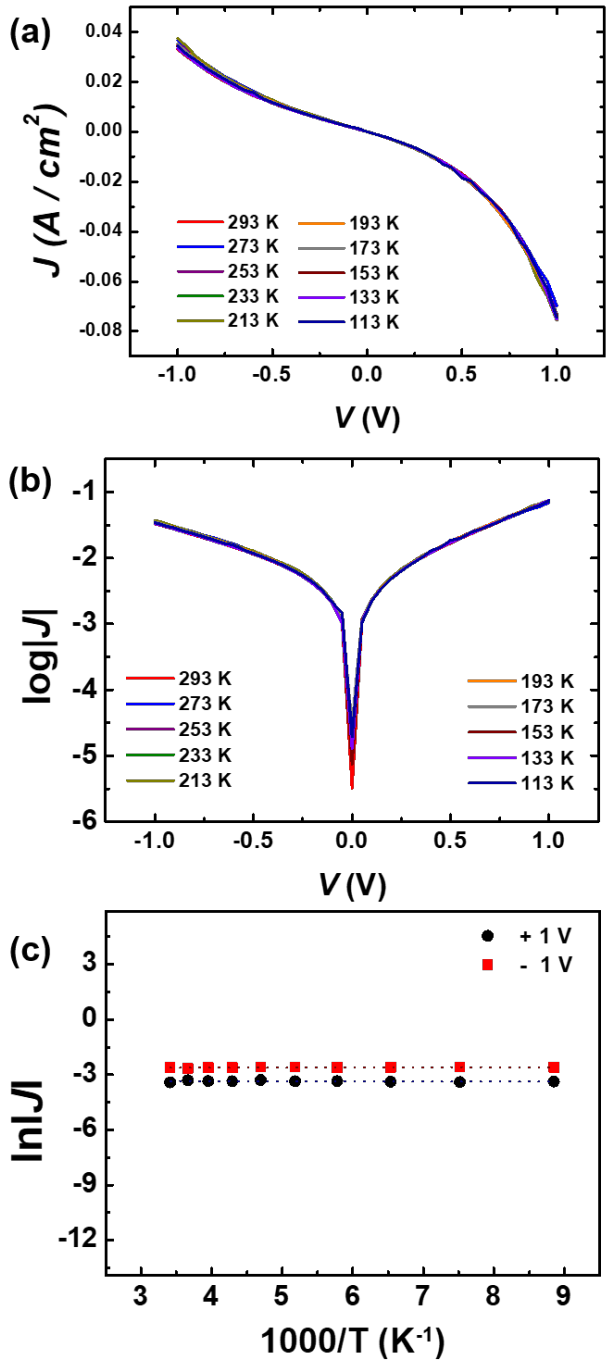

Figure S3. Data of low temperature (from 113 to 293 K) experiments for $Au^{TS}/NHC(Ph)_1//Ga_2O_3/EGaIn$ junction. a) *J-V* traces measured at ±1.0 V; (b) log|*J*|-V traces measured at ±1.0 V; (c) the corresponding Arrhenius plot.

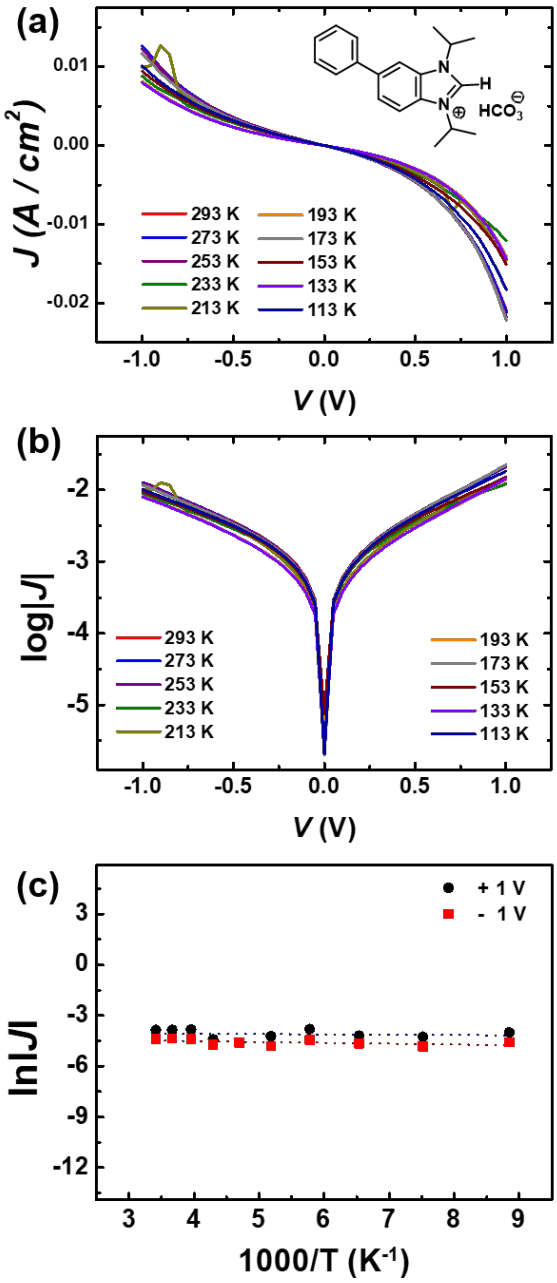

Figure S4. Data of low temperature (from 113 to 293 K) experiments for $Au^{TS}/NHC(Ph)_2//Ga_2O_3/EGaIn$ junction. a) *J-V* traces measured at ±1.0 V; (b) log|*J*|-V traces measured at ±1.0 V; (c) the corresponding Arrhenius plot.

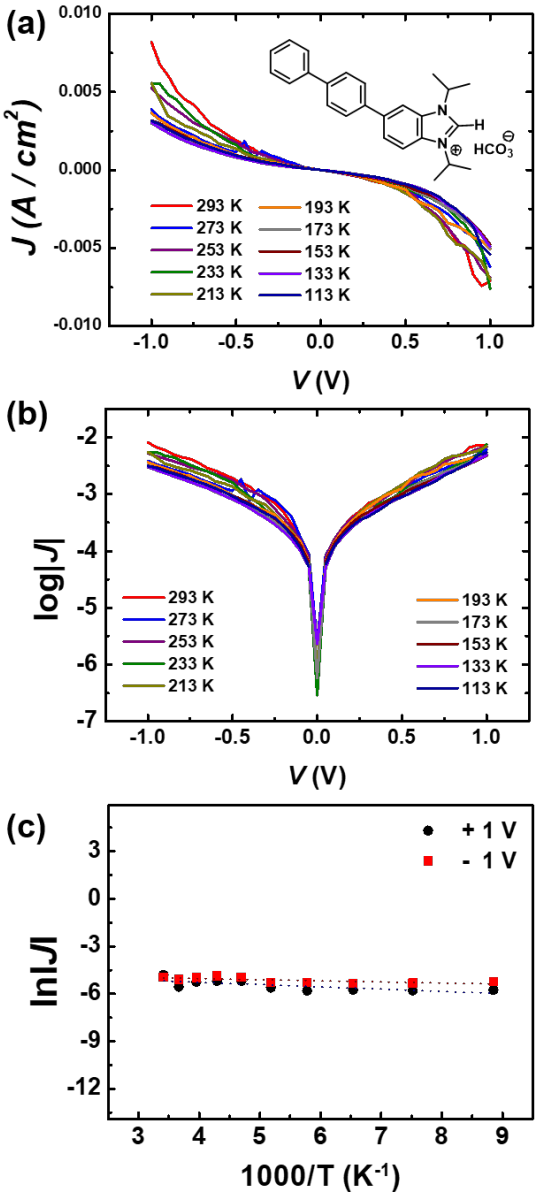

Figure S5. Thermopower analysis of Au^{TS}/SAM//Ga_2O_3/EGaIn junction.

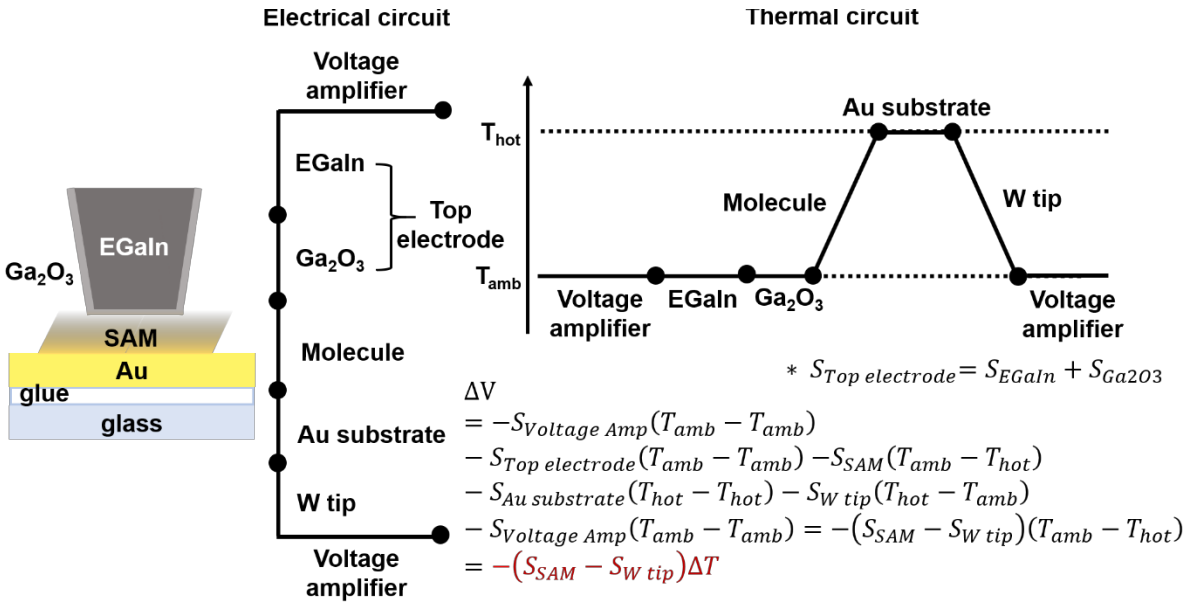

$$* \; S_{Top\ electrode} = S_{EGaIn} + S_{Ga2O3}$$

$$\begin{aligned}\Delta V &= -S_{Voltage\ Amp}(T_{amb} - T_{amb}) \\ &- S_{Top\ electrode}(T_{amb} - T_{amb}) - S_{SAM}(T_{amb} - T_{hot}) \\ &- S_{Au\ substrate}(T_{hot} - T_{hot}) - S_{W\ tip}(T_{hot} - T_{amb}) \\ &- S_{Voltage\ Amp}(T_{amb} - T_{amb}) = -(S_{SAM} - S_{W\ tip})(T_{amb} - T_{hot}) \\ &= -(S_{SAM} - S_{W\ tip})\Delta T\end{aligned}$$

Figure S6. XPS survey spectrum and high resolution spectra (O1s, N1s, Au4f and C1s) for Au^{TS}/NHC(Ph)$_0$ SAM on Au^{TS}.

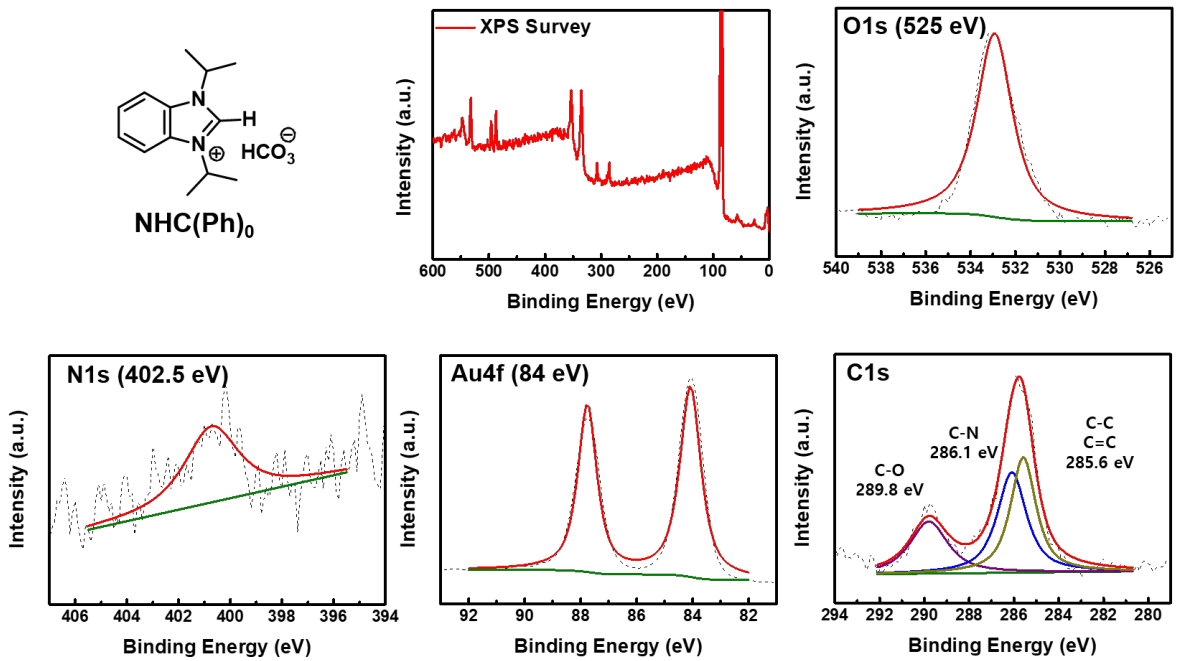

Figure S7. XPS survey spectrum and high resolution spectra (O1s, N1s, Au4f and C1s) for $Au^{TS}/NHC(Ph)_1$ SAM on Au^{TS}.

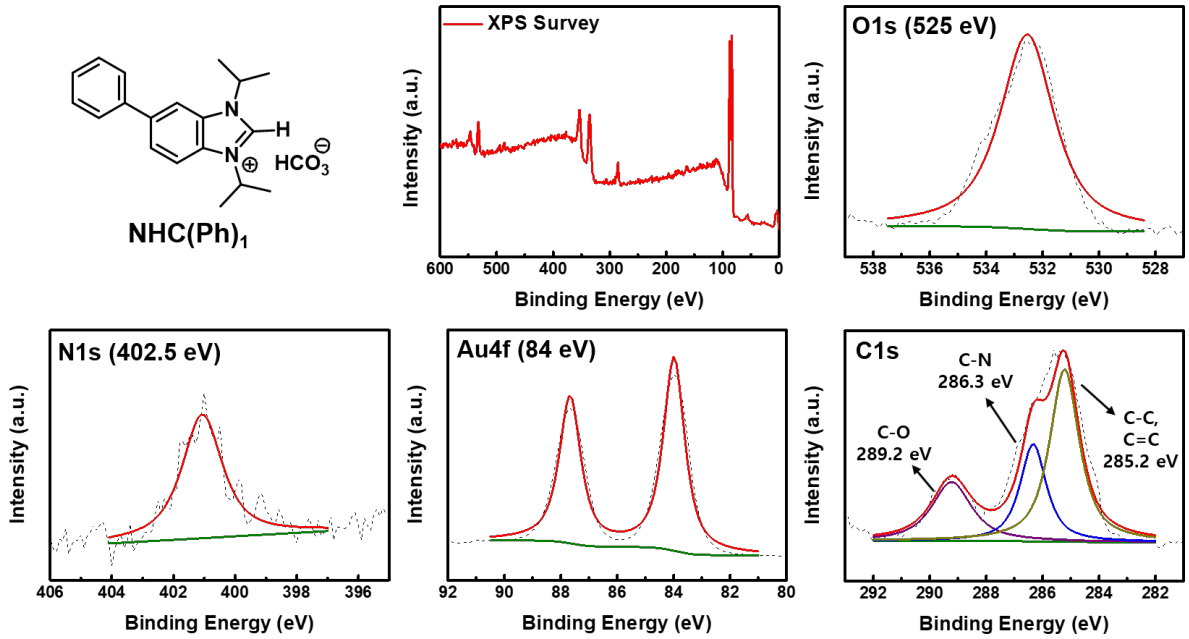

Figure S8. XPS survey spectrum and high resolution spectra (O1s, N1s, Au4f and C1s) for $Au^{TS}/NHC(Ph)_2$ SAM on Au^{TS}.

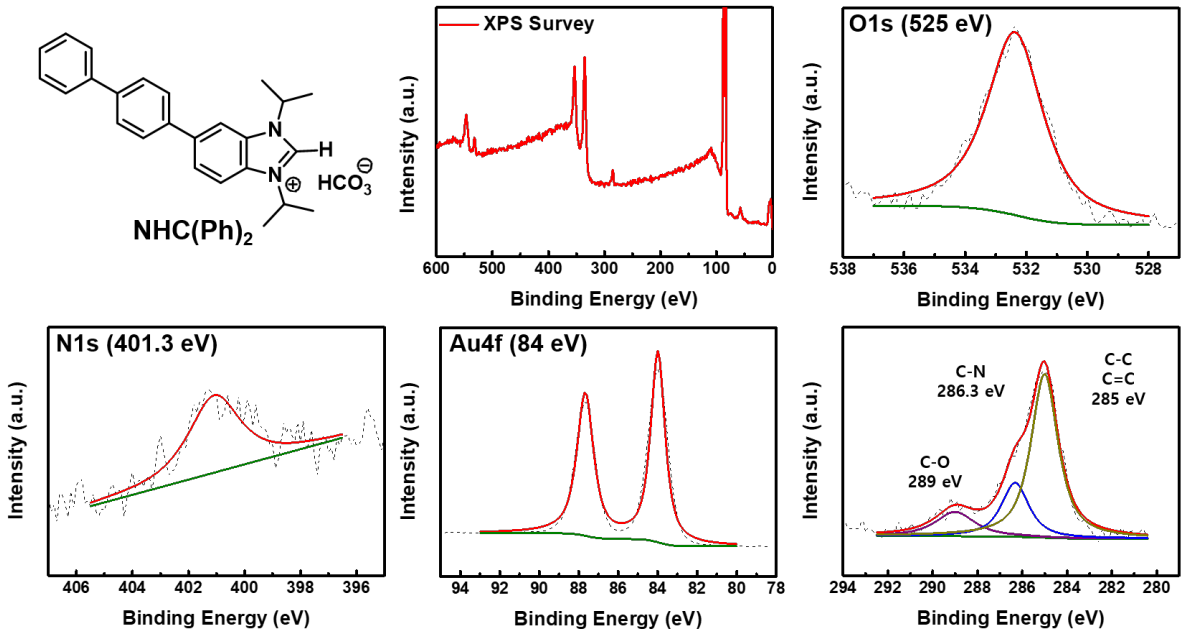

Figure S9. UPS spectra for $Au^{TS}/NHC(Ph)_n$ SAMs. Red and blue solid lines indicate cutoff and onset energies, respectively. Insets show the determination of secondary electron cutoff and onset regions.

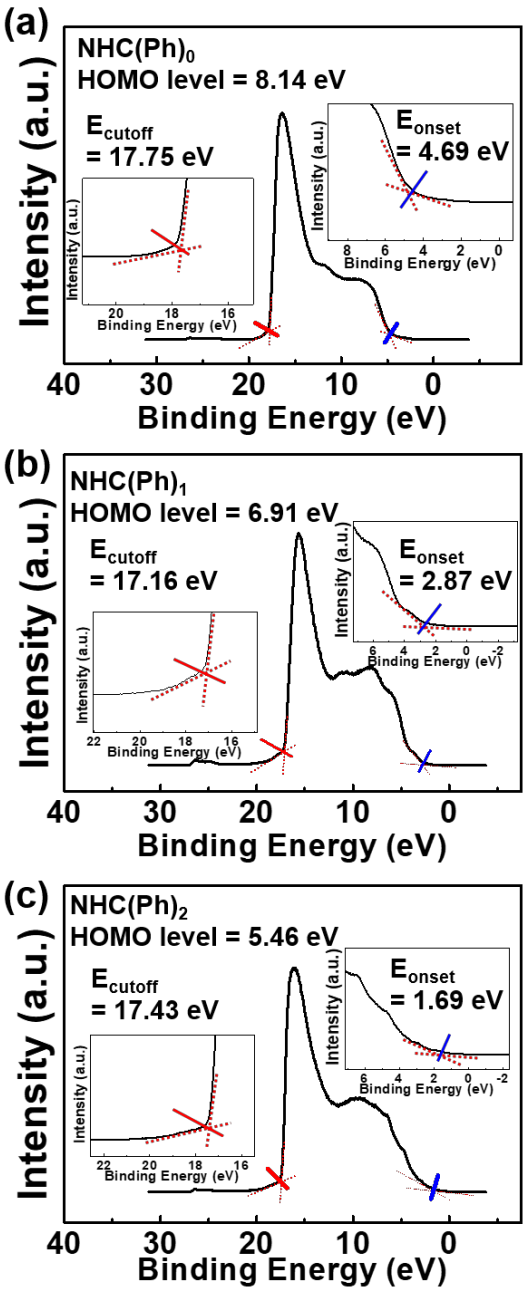

Figure S10. Measurements of static water contact angle for a series of $Au^{TS}/NHC(Ph)_n$ (n=0,1,2) SAMs. The contact angles were averaged from 12 separate measurements.

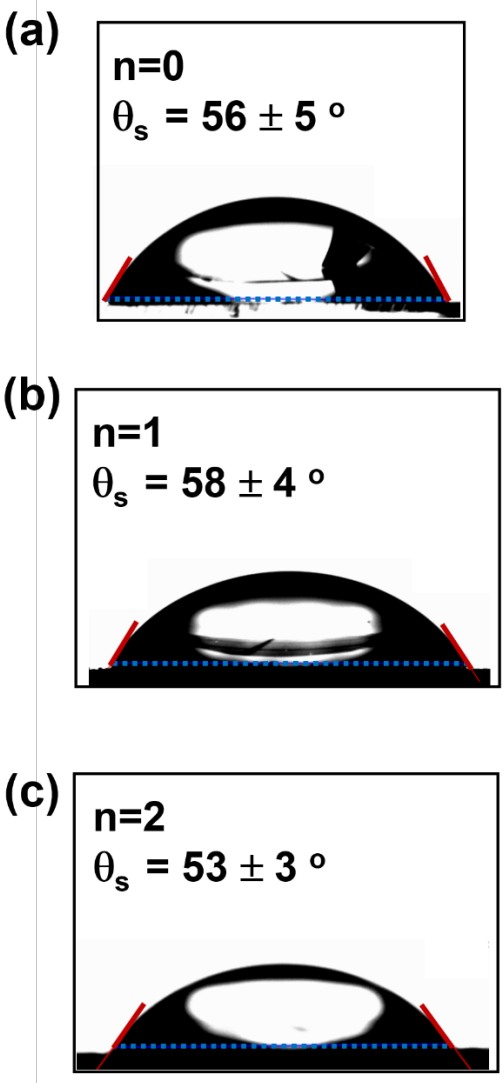

Figure S11. AFM topography and KPFM images of $NHC(Ph)_n$ (n=0,1,2) SAMs on Au^{TS}.

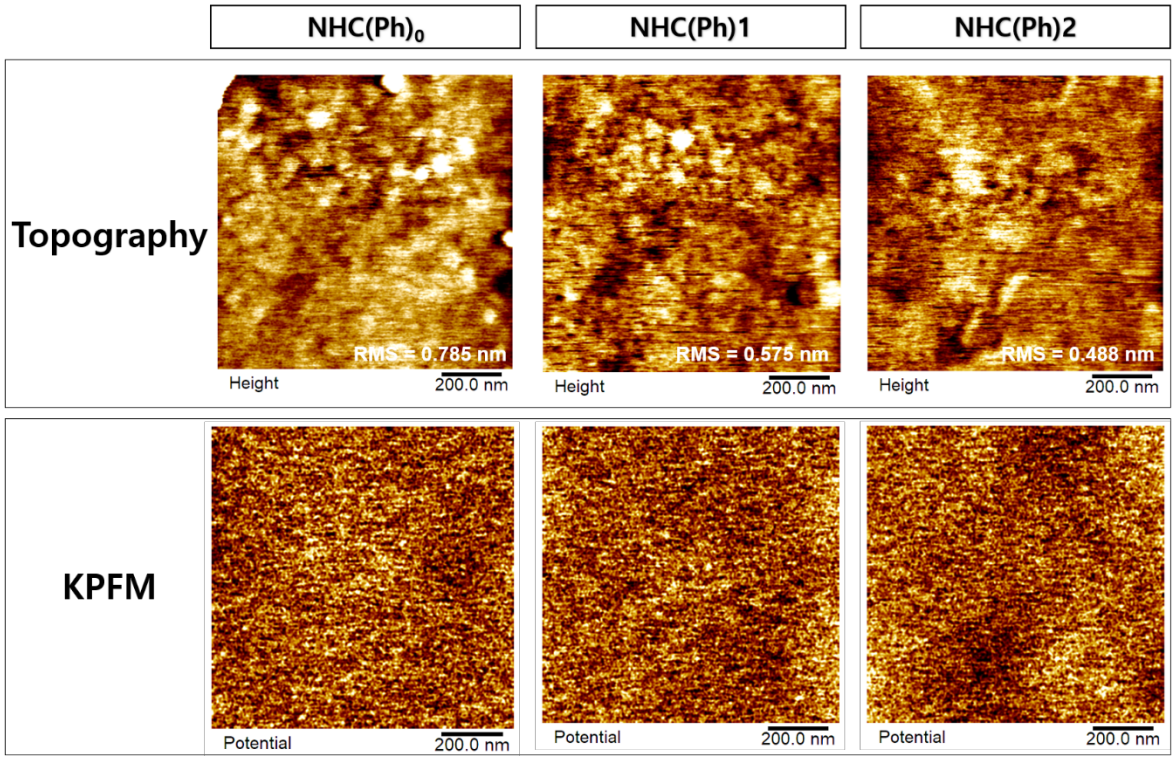

Figure S12. (a) Static contact angle and dynamic contact angle data for Au^{TS}/$NHC(Ph)_n$ SAMs. (b) Work function (WF) of $NHC(Ph)_n$ SAM-bound Au^{TS} chips measured by KPFM and UPS.

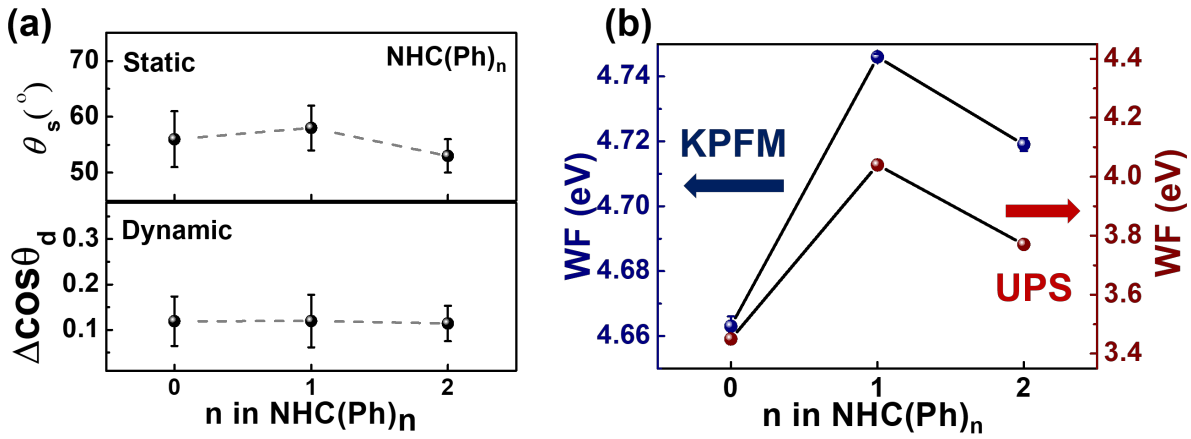

Figure S13. Histograms of thermoelectric voltage measured on Au^{TS}/SAM//Ga_2O_3/EGaIn junctions, and estimated mean and sigma (standard deviation) values from Gaussian fitting curves. SAM was composed of $NHC(Ph)_n$ (n=0,1,2).

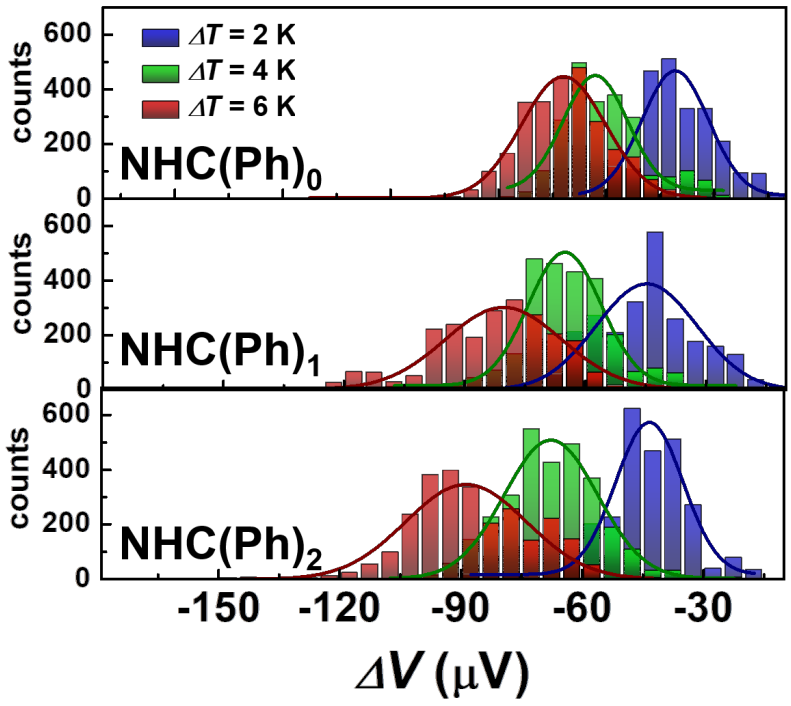

Figure S14. (a) Transmission function coefficient ($T(E)$) of HOMO energy levels (ε_{HOMO}) estimated by UPS for $NHC(Ph)_n$ monolayers (n=0,1,2). Inset shows the plot of energy offset between Fermi level (E_F) of electrode and ε_{HOMO} as a function of the molecular length (n in $NHC(Ph)_n$). (b) Exemplary data of fitting of measured $\log|J|$-V trace with transmission function and Laudauer formula.

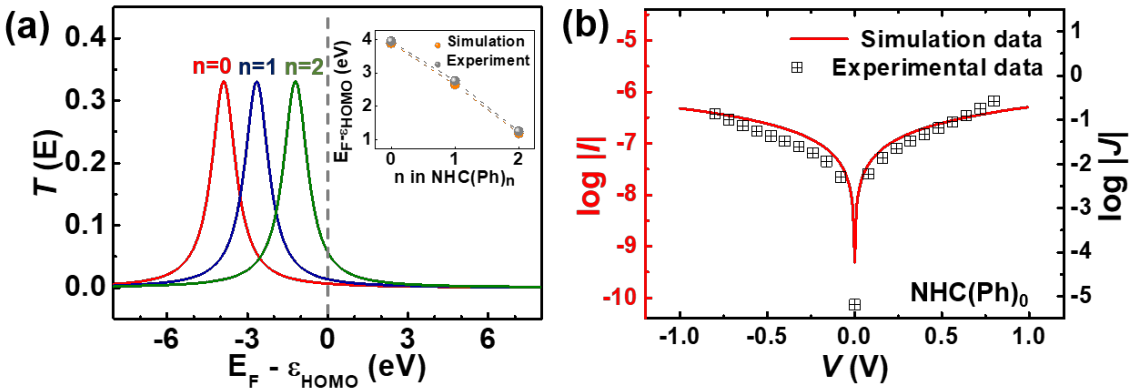

Figure S15. ^{1}H and ^{13}C NMR, and HRMS spectra

^{1}H NMR spectrum of S4

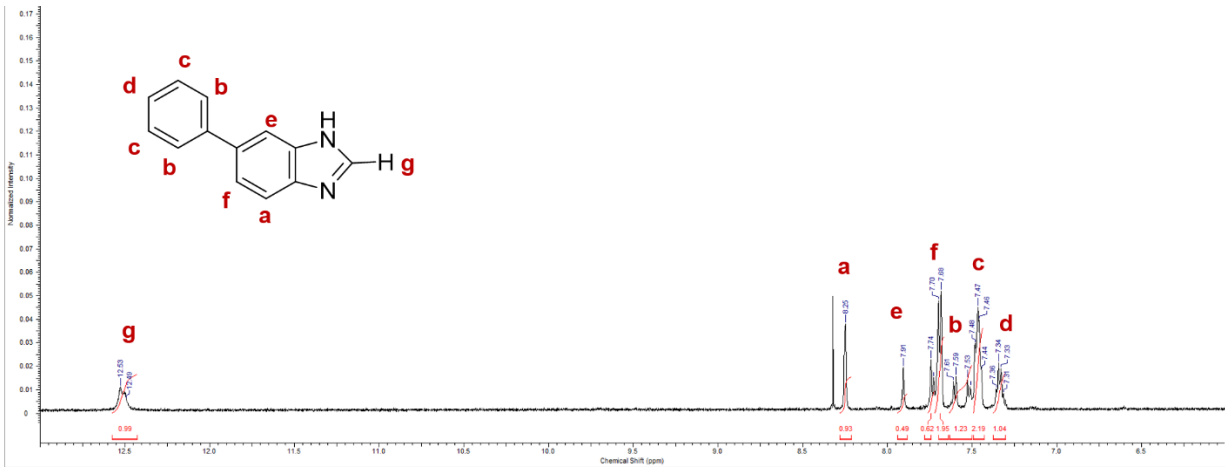

^{13}C NMR spectrum of S4

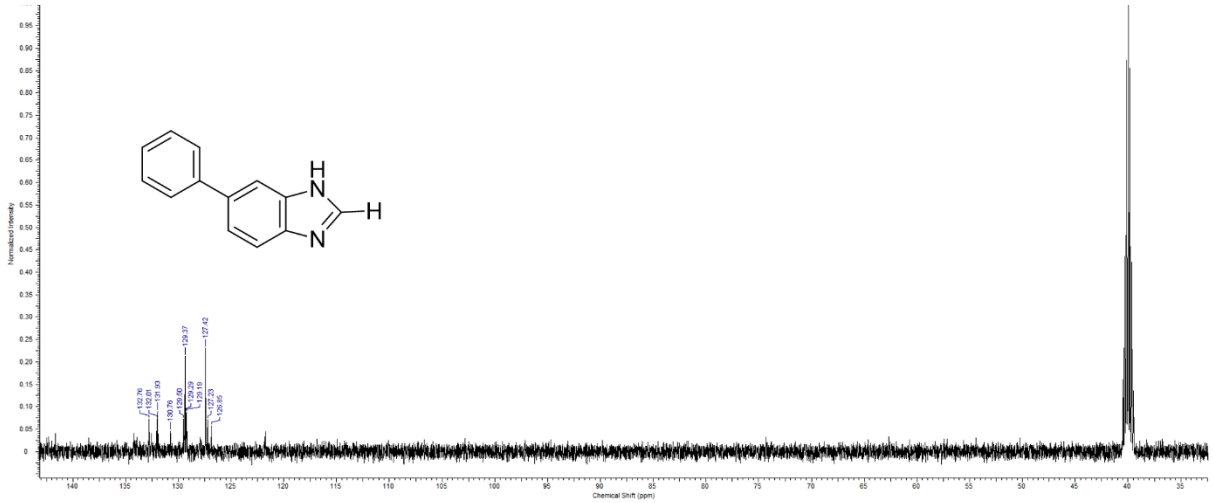

MS spectrum of S4

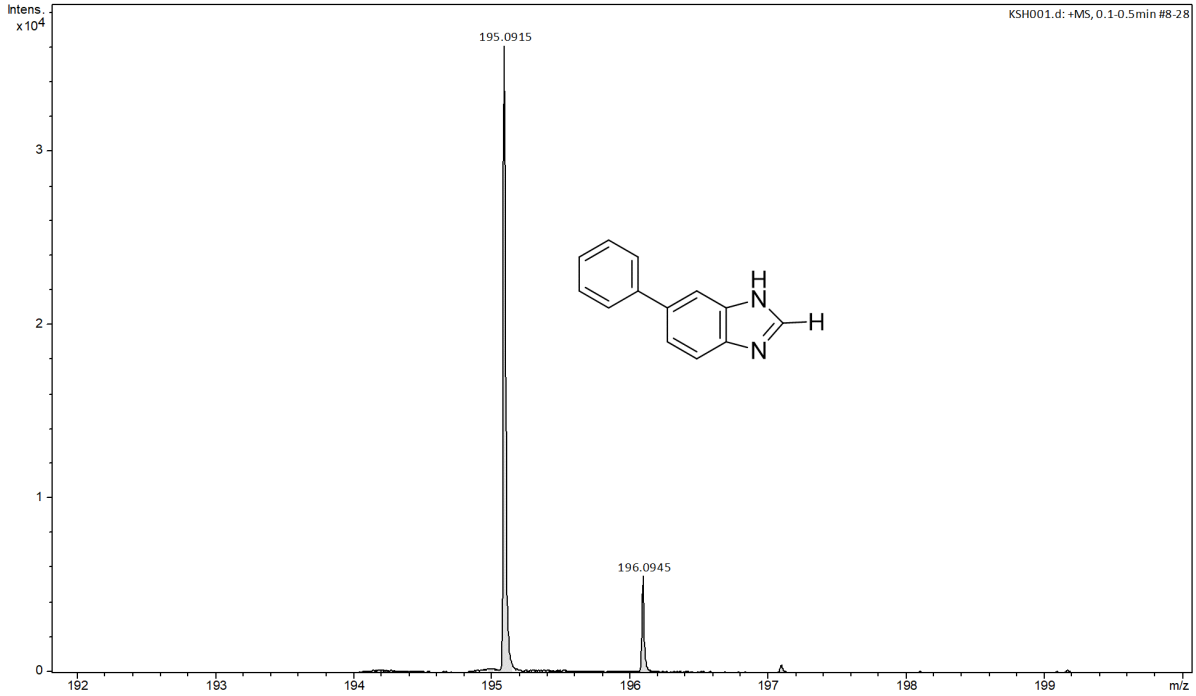

^{1}H NMR spectrum of S5

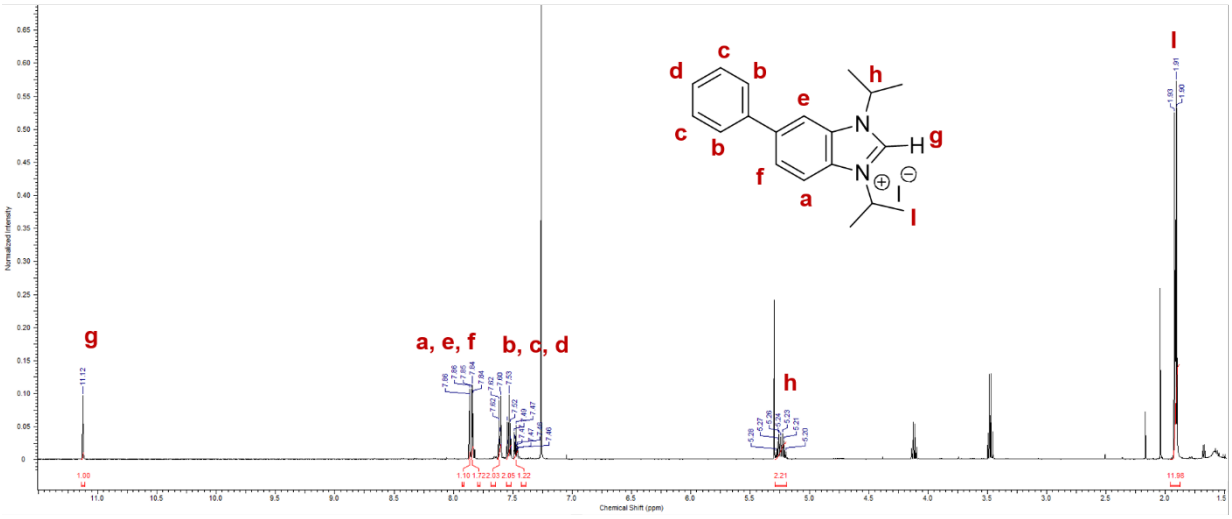

^{13}C NMR spectrum of S5

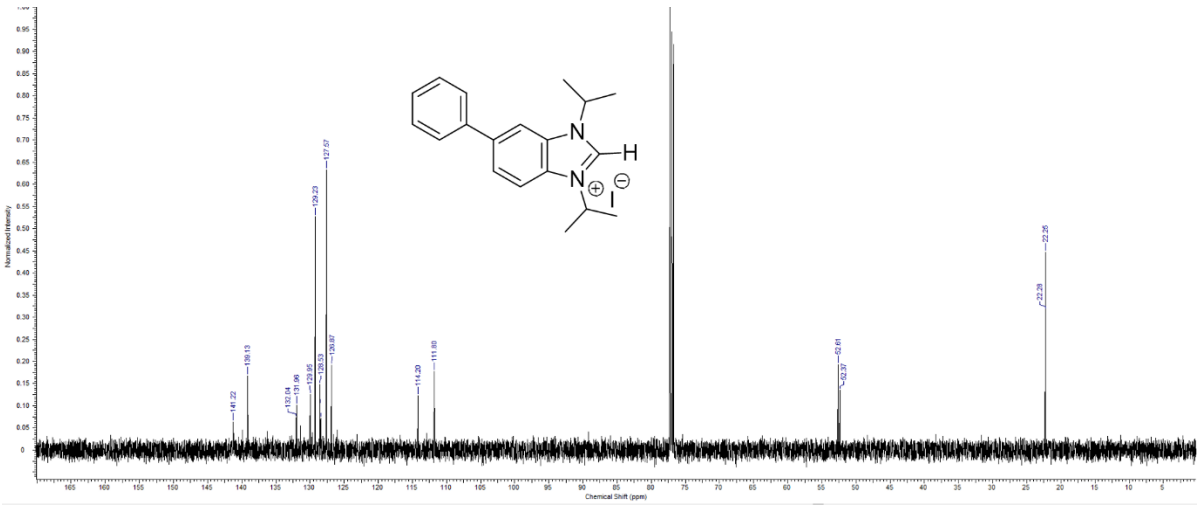

MS spectrum of S5

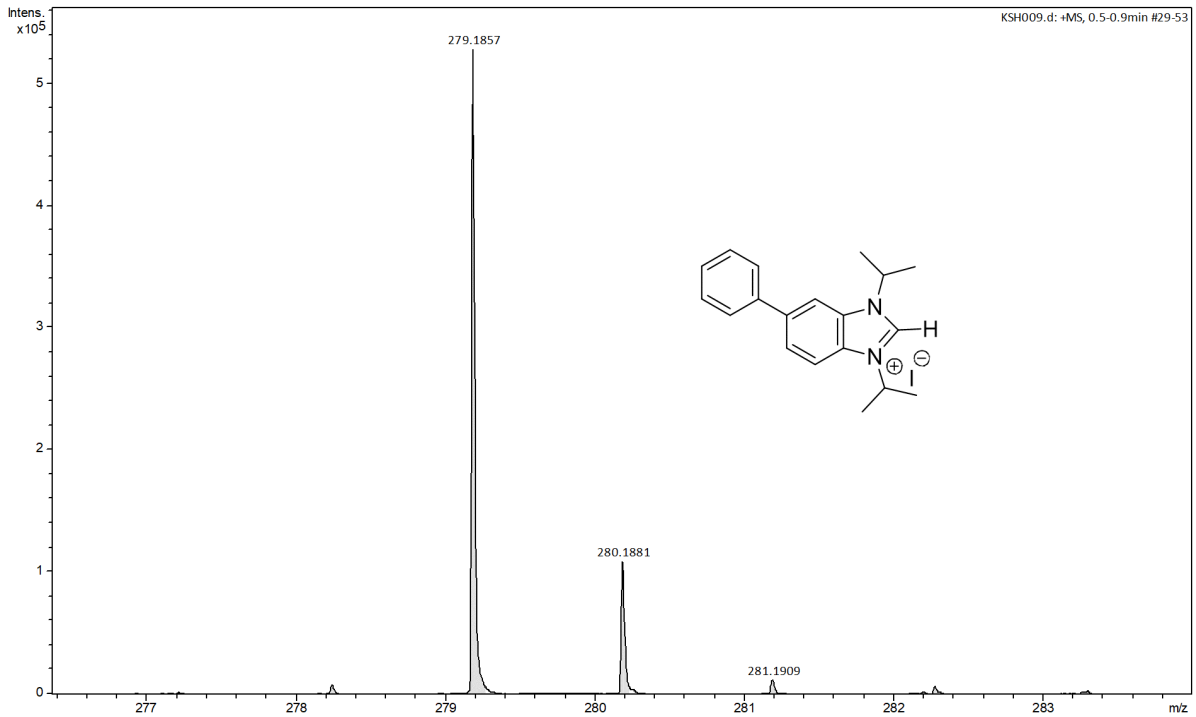

^{1}H NMR spectrum of S6

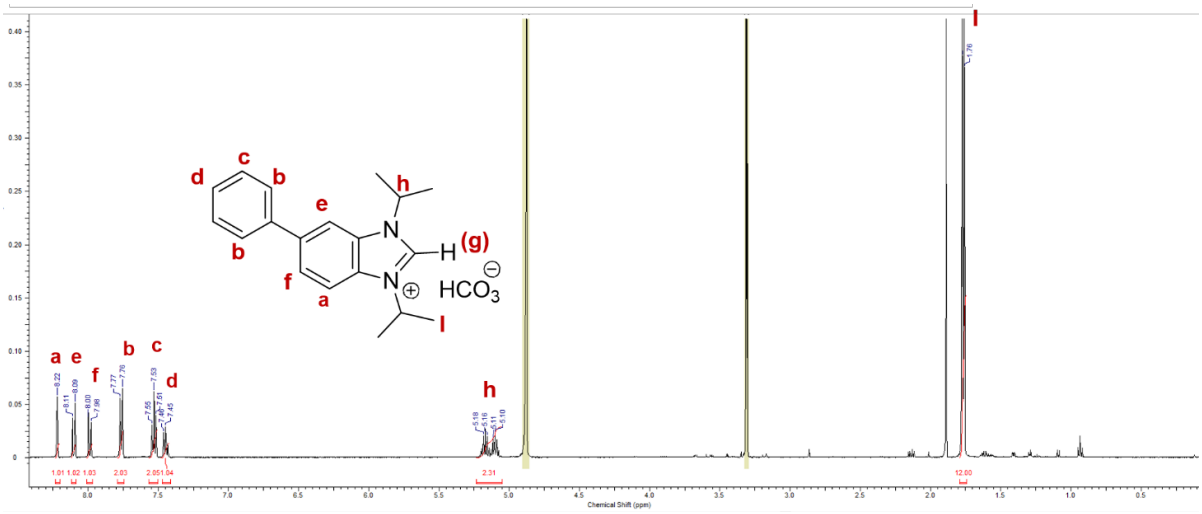

^{13}C NMR spectrum of S6

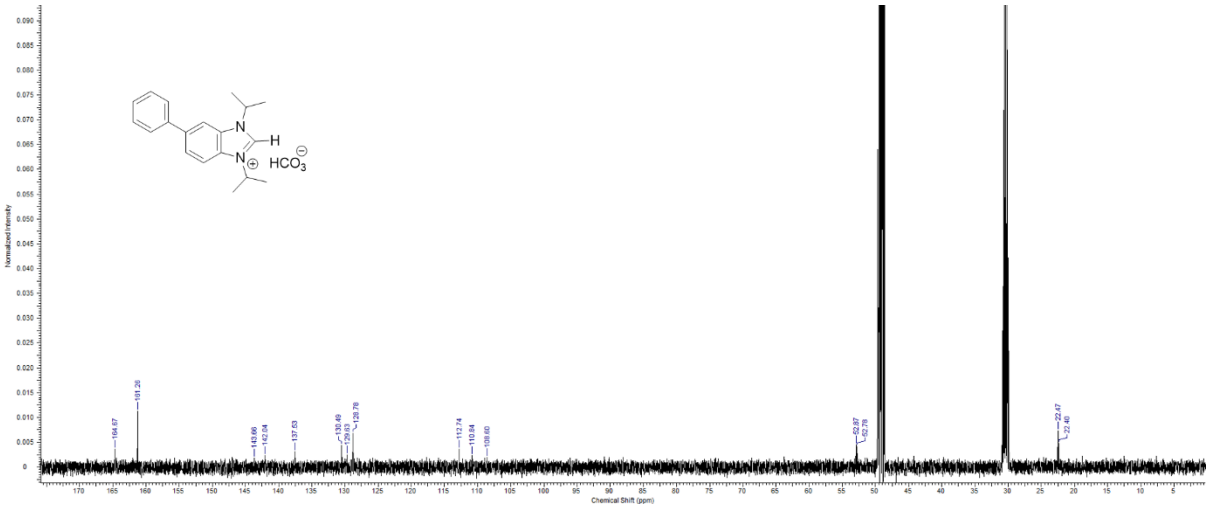

MS spectrum of S6

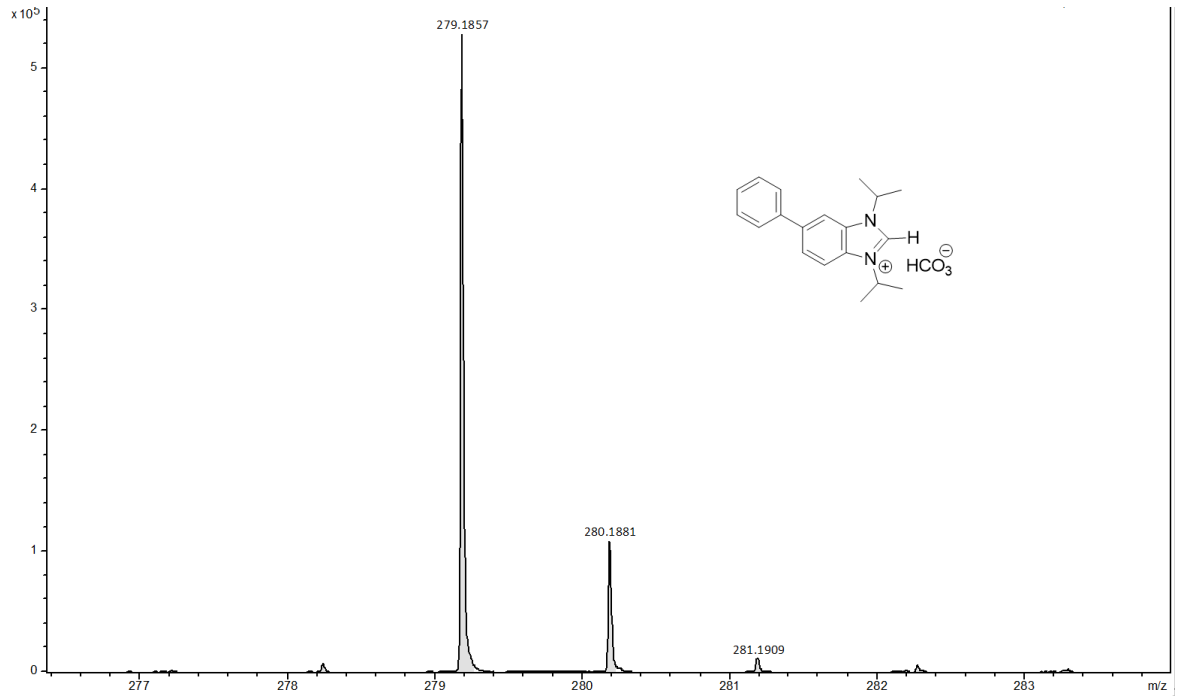

^{1}H NMR spectrum of S7

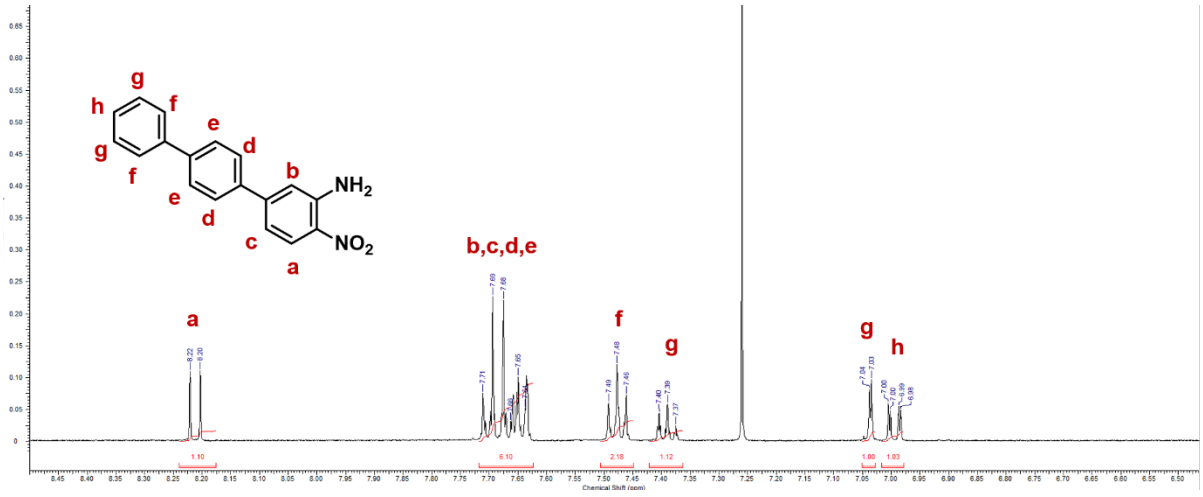

^{13}C NMR spectrum of S7

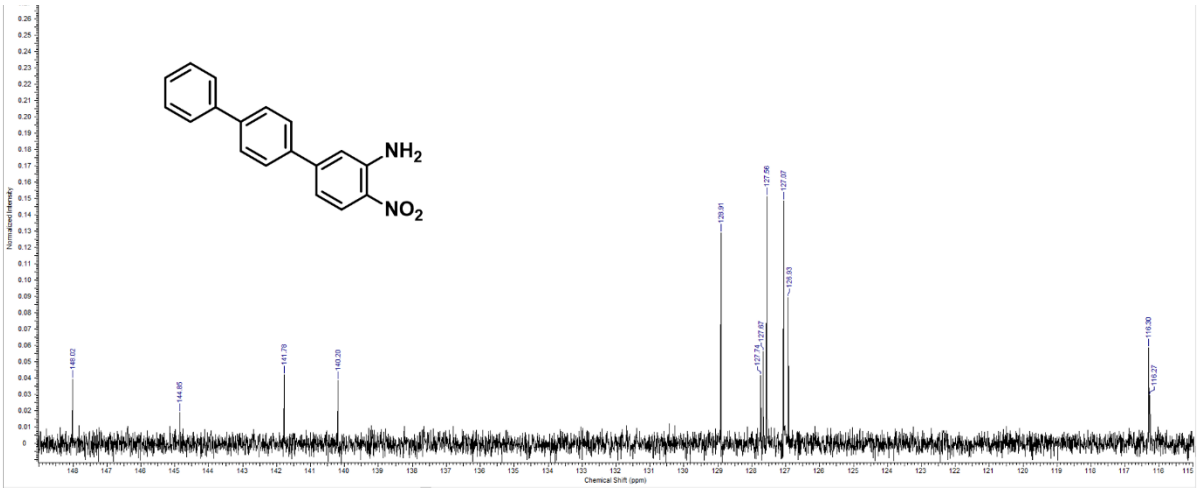

MS spectrum of S7

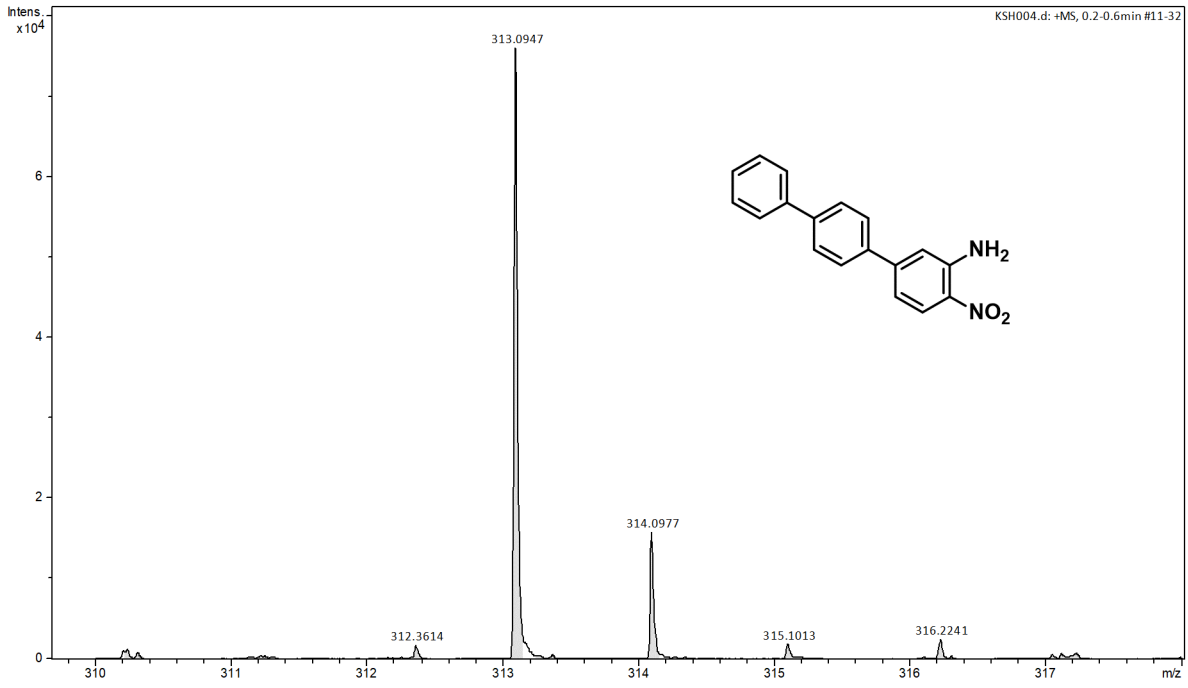

^{1}H NMR spectrum of S8

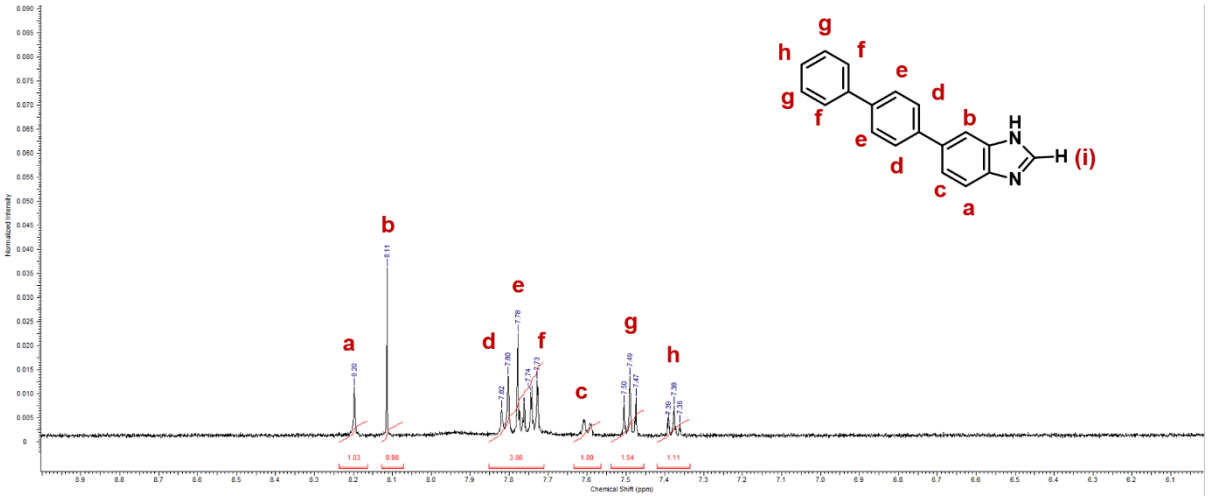

^{13}C NMR spectrum of S8

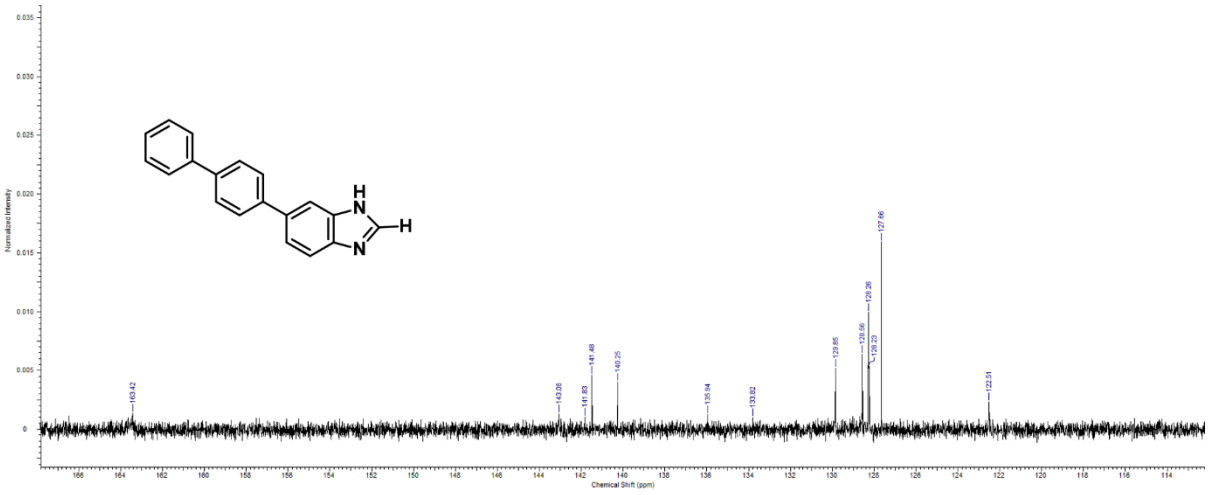

MS spectrum of S8

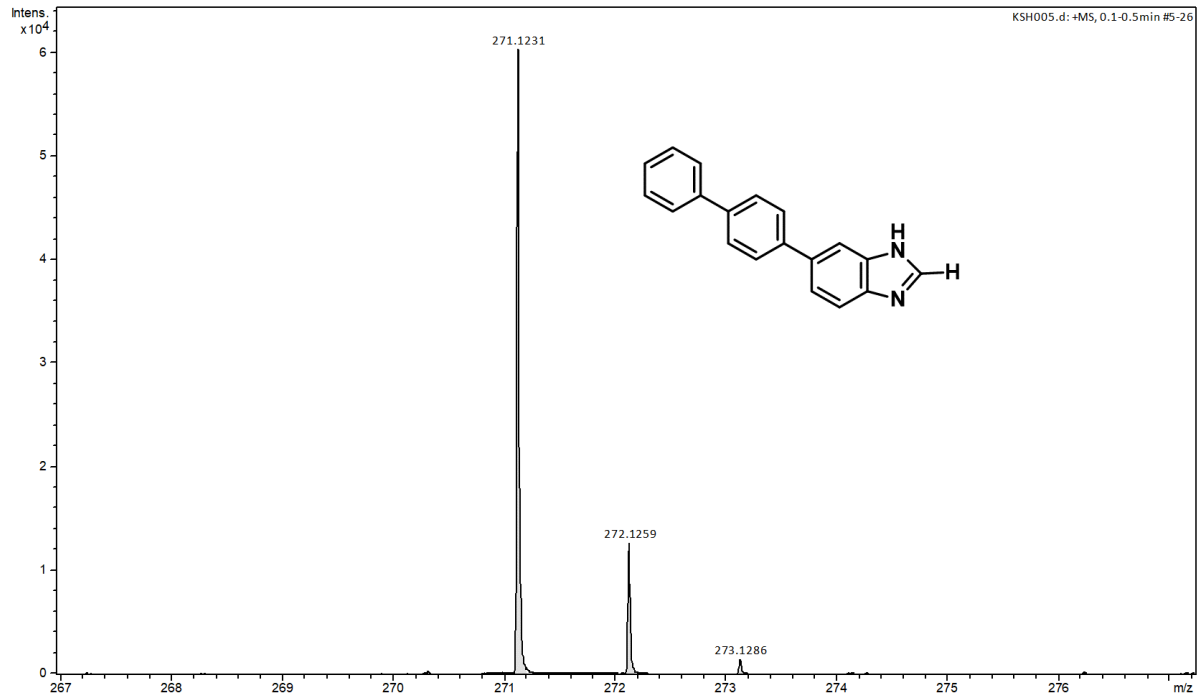

^{1}H NMR spectrum of S9

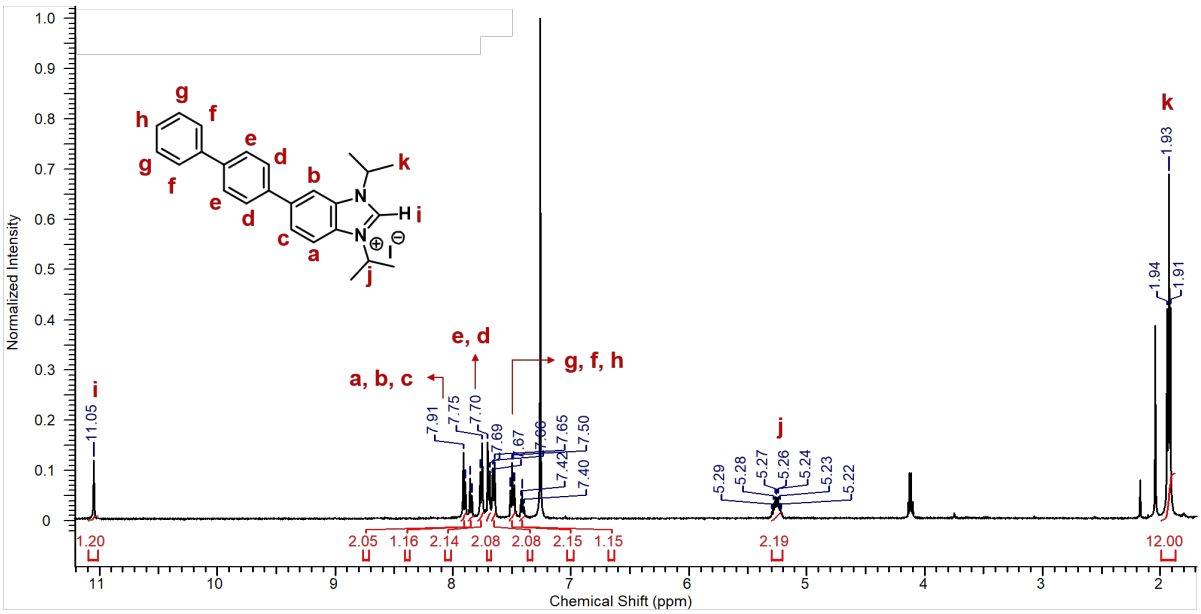

^{13}C NMR spectrum of S9

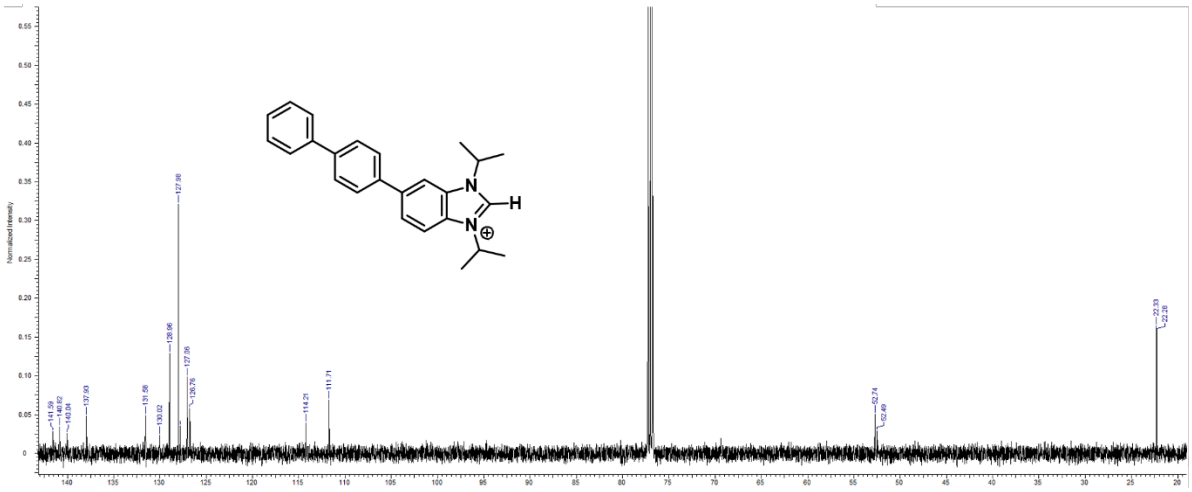

MS spectrum of S9

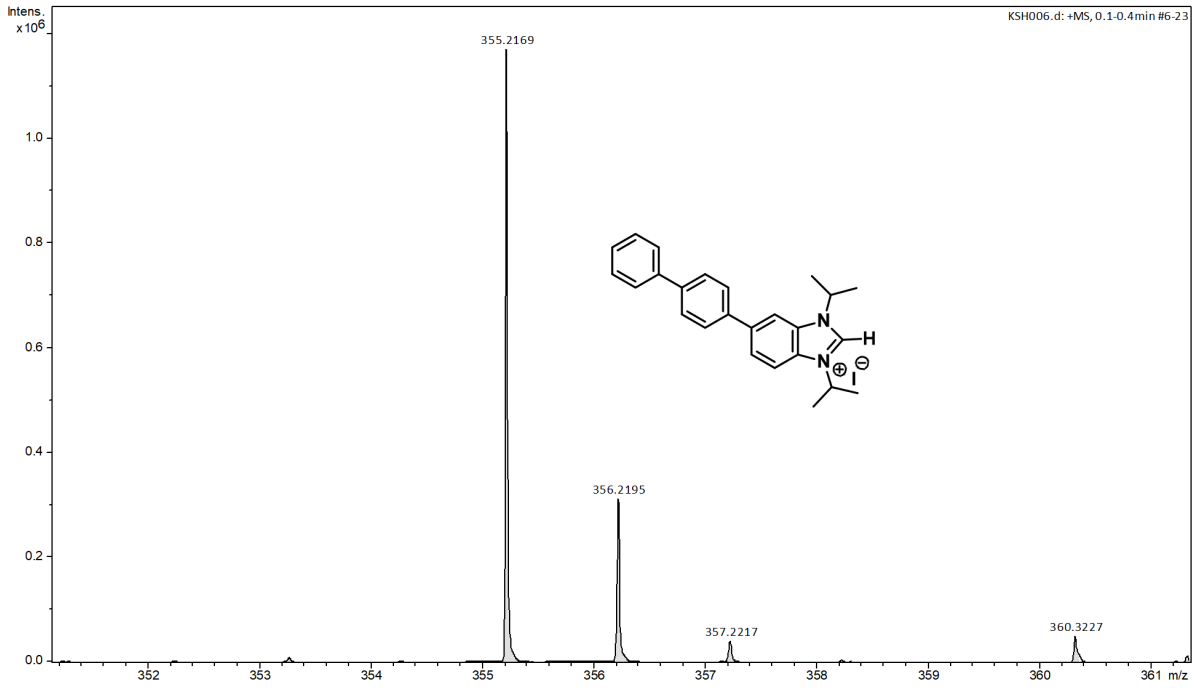

^{1}H NMR spectrum of S10

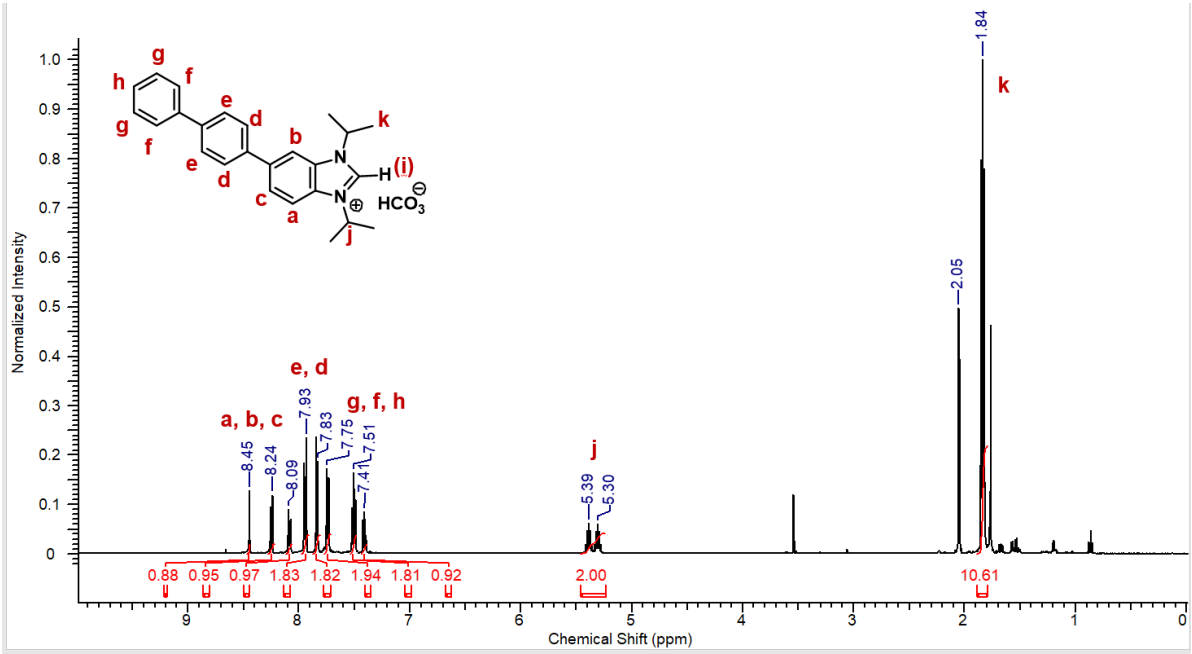

^{13}C NMR spectrum of S10

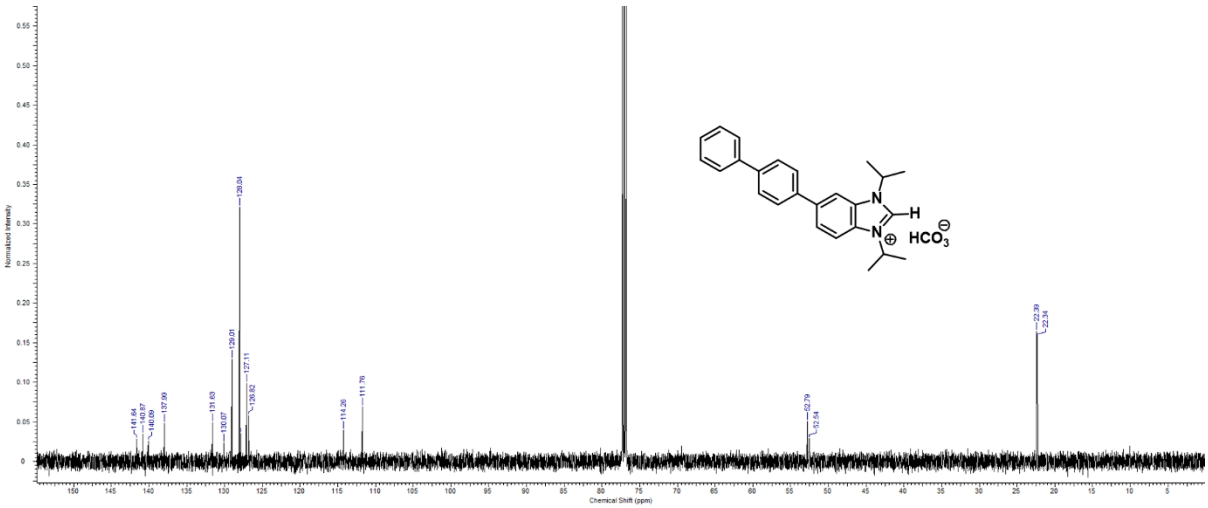

MS spectrum of S10

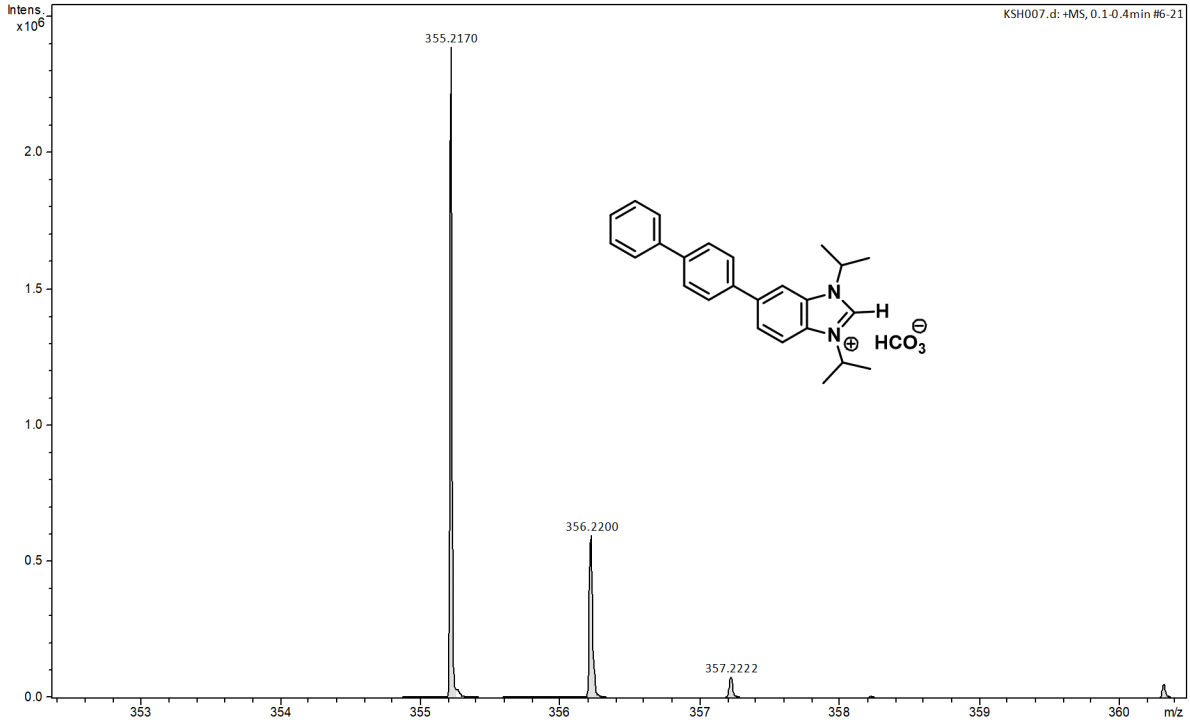

7. References

1. W. C. Chen, Y. C. Lai, W. C. Shih, M. S. Yu, G. P. A. Yap and T. G. Ong, *Chem. Eur. J.*, 2014, **20**, 8099-8015.
2. C. M. Crudden, J. H. Horton, M. R. Narouz, Z. Li, C. A. Smith, K. Munro, C. J. Baddeley, C. R. Larrea, B. Drevniok, B. Thanabalasingam, A. B. McLean, O. V. Zenkina, I. I. Ebralidze, Z. She, H.-B. Kraatz, N. J. Mosey, L. N. Saunders and A. Yagi, *Nat. Commun.*, 2016, **7**, 12654.
3. E. A. Doud, M. S. Inkpen, G. Lovat, E. Montes, D. W. Paley, M. L. Steigerwald, H. Vázquez, L. Venkataraman and X. Roy, *J. Am. Chem. Soc.*, 2018, **140**, 8944–8949.
4. J. E. Wulff, R. Siegrist and A. G. Myers, *J. Am. Chem. Soc.*, 2007, **129**, 14444-14451.
5. C. M. Crudden, J. H. Horton, I. I. Ebralidze, O. V. Zenkina, A. B. McLean, B. Drevniok, Z. She, H.-B. Kraatz, N. J. Mosey, T. Seki, E. C. Keske, J. D. Leake, A. Rousina-Webb and G. Wu, *Nat. Chem.*, 2014, **6**, 409–414.
6. F. C. Simeone, H. J. Yoon, M. M. Thuo, J. R. Barber, B. Smith and G. M. Whitesides, *J. Am. Chem. Soc.*, 2013, **135**, 18131-18144.
7. G. D. Kong, M. Kim, S. J. Cho and H. J. Yoon, *Angew. Chem., Int. Ed.*, 2016, **55**, 10307-10311.
8. S. E. Byeon, M. Kim and H. J. Yoon, *ACS Appl. Mater. Interfaces*, 2017, **9**, 40556-40563.
9. S. Park and H. J. Yoon, *Nano Lett.*, 2018, **18**, 7715–7718.
10. P. Reddy, S.-Y. Jang, R. A. Segalman and A. Majumdar, *Science*, 2007, **315**, 1568-1571.
11. S. K. Yee, J. A. Malen, A. Majumdar and R. A. Segalman, *Nano Lett.*, 2011, **11**, 4089–4094.
12. M. Büttiker, Y. Imry, R. Landauer and S. Pinhas, *Phys. Rev. B*, 1985, **31**, 6207.
13. M. Paulsson and S. Datta, *Phys. Rev. B*, 2003, **67**, 241403.
14. M. Brandbyge, J.-L. Mozos, P. Ordejón, J. Taylor and K. Stokbro, *Phys. Rev. B*, 2002, **65**, 165401.
15. Z.-L. Cheng, R. Skouta, H. Vazquez, J. R. Widawsky, S. Schneebeli, W. Chen, M. S. Hybertsen, R. Breslow and L. Venkataraman, *Nat. Nanotechnol.*, 2011, **6**, 353–357.
16. S. J. Cho, G. D. Kong, S. Park, J. Park, S. E. Byeon, T. Kim and H. J. Yoon, *Nano Lett.*, 2019, **19**, 545-553.
17. Z. Xie, I. Bâldea and C. D. Frisbie, *Chem. Sci.*, 2018, **9**, 4456-4467.
18. K. Baheti, J. A. Malen, P. Doak, P. Reddy, S.-Y. Jang, T. D. Tilley, A. Majumdar and R. A. Segalman, *Nano Lett.*, 2008, **8**, 715–719.
19. A. Tan, J. Balachandran, S. Sadat, V. Gavini, B. D. Dunietz, S.-Y. Jang and P. Reddy, *J. Am. Chem. Soc.*, 2011, **133**, 8838–8841.
20. P. N. Butcher, *J. Phys. Condens. Matter*, 1990, **2**, 4869−4878.
21. G. Lovat, E. A. Doud, D. Lu, G. Kladnik, M. S. Inkpen, M. L. Steigerwald, D. Cvetko, M. S. Hybertsen, A. Morgante, X. Roy and L. Venkataraman, *Chem. Sci.*, 2019, **10**, 930-935.
22. H. K. Kim, A. S. Hyla, P. Winget, H. Li, C. M. Wyss, A. J. Jordan, F. A. Larrain, J. P. Sadighi, C. Fuentes-Hernandez, B. Kippelen, J.-L. Bredas, S. Barlow and S. R. Marder, *Chem. Mater.*, 2017, **29**, 3403−3411.
23. H. J. Yoon, C. M. Bowers, M. Baghbanzadeh and G. M. Whitesides, *J. Am. Chem. Soc.*, 2014, **136**, 16-19.
24. O. Gershevitz, C. N. Sukenik, J. Ghabboun and D. Cahen, *J. Am. Chem. Soc.*, 2003, **125**, 4730–4731.
25. L. Romaner, G. Heimel, C. Ambrosch-Draxl and E. Zojer, *Adv. Funct. Mater.*, 2008, **18**, 3999-4006.
26. H. J. Yoon, N. D. Shapiro, K. M. Park, M. M. Thuo, S. Soh and G. M. Whitesides, *Angew. Chem., Int. Ed.*, 2012, **51**, 4658-4661.
27. C. M. Bowers, K.-C. Liao, H. J. Yoon, D. Rappoport, M. Baghbanzadeh, F. C. Simeone and G. M. Whitesides, *Nano Lett.*, 2014, **14**, 3521-3526.
28. K. C. Liao, H. J. Yoon, C. M. Bowers, F. C. Simeone and G. M. Whitesides, *Angew. Chem., Int. Ed.*, 2014, **53**, 3889-3893.

29. G. D. Kong, M. Kim, H. J. Jang, K. C. Liao and H. J. Yoon, *Phys. Chem. Chem. Phys.*, 2015, **17**, 13804-13807.